UNIVERSIDADE D
COIMBRA

André Filipe Almeida Simões

Depth-resolved information in muon implantation experiments in films

Dissertação no âmbito do Mestrado Integrado em Engenharia Física, ramo de Instrumentação,
orientada pela Professora Doutora Maria Helena Vieira Alberto
e pelo Professor Doutor Rui César do Espírito Santo Vilão
e apresentada ao Departamento de Física da Faculdade de Ciências e Tecnologia
da Universidade de Coimbra.

Julho de 2019

Resumo

O objectivo desta tese é desenvolver um método para extrair informação em função da profundidade da amostra, em experiências que usam muões positivos de baixa energia como sondas microscópicas. Esta informação de profundidade é obtida a partir da dependência dos parâmetros experimentais com a energia de implantação do muão. A informação dependente da energia contém informação sobre diferentes efeitos numa certa amostra, contudo, é crucial inferir a posição espacial em que os efeitos ocorrem e a sua extensão.

Quatro heteroestruturas semicondutoras compostas por cádmio, índio, gálio, selénio (CIGS), geralmente usado em células fotovoltaicas, foram usadas para exemplificar este método. As medidas com muões lentos foram obtidas no instrumento *Low Energy Muon* (LEM), no Paul Scherrer Institut (PSI), na Suíça, com um feixe de muões com energias de implantação que variam de 1 a 30 keV, permitindo o controlo da profundidade média de implantação dos muões nas amostras. A análise possibilitada por esta ferramenta permite desvendar detalhes microscópicos da interface dos semicondutores, abrindo o caminho para uma modelação física adequada das suas propriedades.

Palavras-chave: muões lentos, espectroscopia do muão, CIGS

Abstract

The goal of this thesis is to develop a method for extracting depth-resolved information from the muon probe in low energy muon experiments, where muon spin spectroscopy (μSR) is used. This depth-resolved information is to be obtained from the implantation energy dependence of the experimental parameters in the experiment. The energy dependent data is able to identify different effects in a given sample, but it is crucial to infer the spacial position and depth extent of these effects inside the sample in order to better understand them, hence the need for this tool.

Four semiconductor heterostructures with cadmium indium gallium selenide (CIGS), commonly used in photovoltaic cells, were used to exemplify the method. The muon experiments took place in the Low Energy Muon (LEM) facility at the Paul Scherrer Institut (PSI), in Switzerland, with a muon beam ranging from 1 - 30 keV, allowing the control of the average implantation depth of the muons inside the samples. The analysis allowed by the new tool unveils microscopic details of the semiconductor interface, opening the way for adequate physical modelling of its properties.

Keywords: low energy muons, muon spin spectroscopy, CIGS

List of Figures

List of Tables

Contents

Chapter 1

Introduction

1.1 Photovoltaic energy

The always growing global population that translates to an increased global energy demand, together with an enhanced environmental awareness are the factors which have contributed the most for the development of renewable energy sources. However, the progress is very much uneven for the different regions of the world, as energy production and access rates remain very low for many underdeveloped countries, urging for cost-efficient and specific energy solutions that can tackle these issues.

Despite the increase in renewables, fossil fuels continue to hold the overwhelming fraction of the global total energy production and consumption, with renewable electricity only accounting for around 26.5% (Fig 1.1.1) of the global electricity production by the end of 2017 [REN18].

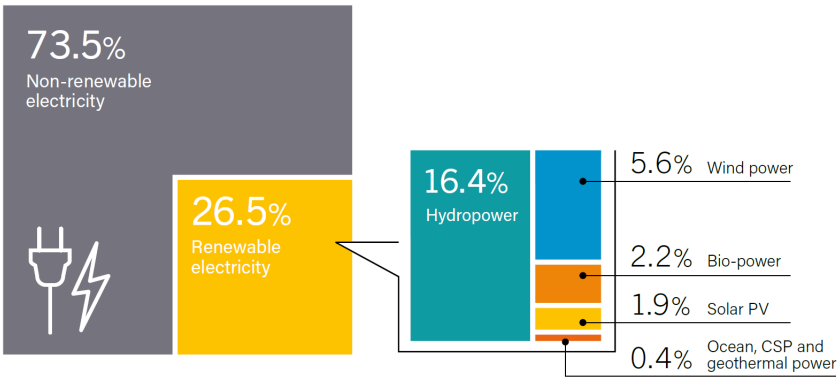

Fig. 1.1.1. Estimated renewable energy share of global electricity production by end-2017 (from [REN18]).

Since the big kickstart in the growth of the photovoltaic (PV) industry in the 1980s, production of photovoltaic modules has been increasing exponentially, with the last decade seeing an extremely rapid evolution in these numbers. In 2017 solar photovoltaics had a landmark year [REN18], seeing its world capacity increase (Fig. 1.1.2) more than any other energy generation technology, having reached in 2018 a global installed capacity value that was around 500GW_p[1][IEA19].

The main contributor to the global expansion of photovoltaics has been China, which is the country that holds the biggest share of the PV market (Fig. 1.1.2) by a large margin, be it terms of photovoltaic module production or installations, eclipsing big western markets like the United States and Germany. With the additional contribution of countries like India and Japan, this makes Asia the leader of the global photovoltaic market [REN18].

[1]Watt-peak (Wp) is used to rate photovoltaic systems. It is the direct current (DC) output of a device under standard test conditions designed to simulate full direct sunshine.

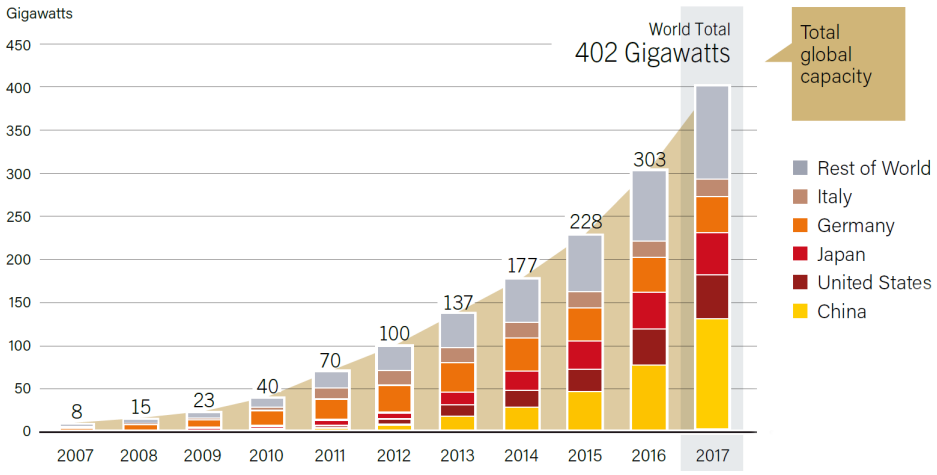

Fig. 1.1.2. Solar PV global capacity, by country or region, from 2007 to 2017. The data is provided in direct current (DC). From [REN18].

Compared to fossil-fuel electricity generation, photovoltaic technology spares the atmosphere of a very significant amount of greenhouse gas emissions during its life-cycle [WNA11], making its research towards reducing manufacturing costs and installation costs per watt cell capacity, while improving cell efficiency, a key strategy towards achieving the decarbonization goals proposed by the Paris Agreement.

1.1.1 Basic working principle of a solar cell

The working principle of a solar cell is analogous to that of a photodiode, that is, of a semiconductor p-n junction (Fig. 1.1.3), yet these are optimized to obtain optimum electric power efficiency from incident sunshine radiation.

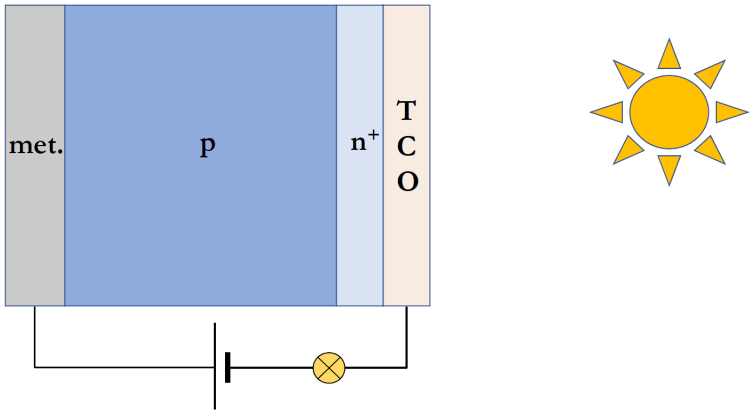

Fig. 1.1.3. Diagram of a solar cell based on a semiconductor n^+-p junction (from [Vil19]).

A voltage is applied on the p-n junction thanks to the two conducting contacts, on the back and front, being that the front contact may be replaced by a transparent conductive oxide (TCO) that lets light through, minimizing the light absorption in this region. With the same intent, the n-type semiconductor must also be thin (as must its depletion zone), implying a higher doping. The depletion zone is restricted to the p-type semiconductor where the light absorption occurs, called the absorber.

In a solar cell, electron-hole pairs are produced in the depletion zone, after which the electric field at the p-n junction separates them, accelerating the holes (h) to the p-zone and the electrons (e) to the n-zone (Fig. 1.1.4), effectively generating a photocurrent from n to p, I_L. Some e-h pairs do get lost before conversion due to various recombination mechanisms [WGWC07]. A saturation current, I_S, must also be considered, which corresponds to a current measured with inverse polarization even in the absence of light, also called dark current. This way, the characteristic I-V curve of an illuminated solar cell is described by:

$$I = I_S \left(\exp\left(\frac{eV_{\text{ext}}}{kT} \right) - 1 \right) - I_L \tag{1.1}$$

where e is the elementary charge, V_{ext} is the applied voltage across the (diode) terminals, k is the Boltzmann constant and T is the temperature.

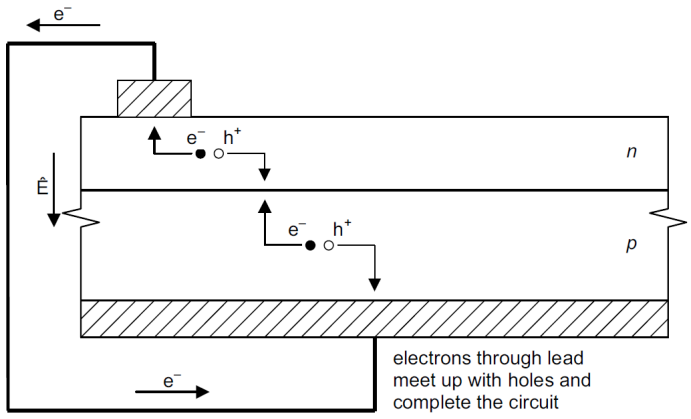

Fig. 1.1.4. Ideal short circuit flow of electrons and holes at the p-n junction (from [WGWC07]).

The parameters used to characterize the output (performance) of a solar cell, given the intrinsic and operational characteristics of the solar cell are:

- **Short circuit current (I_{sc}):** The maximum current that flows through the external circuit at zero voltage, that is, when the electrodes of the cell are short circuited. It depends on the area of the cell, and is directly proportional to the incident sunlight.

- **Open circuit voltage (V_{oc}):** The maximum voltage with zero current through the external circuit. It increases logarithmically with incident sunlight.

  For $I = 0$, that is, when the dark current compensates the photocurrent, from equation 1.1 one can obtain:

$$V_{oc} = \frac{kT}{e} \ln\left(\frac{I_L}{I_S} + 1\right) \tag{1.2}$$

  This quantity depends on the saturation current I_S and photogenerated current I_L, yet, of these two, I_S exhibits significantly bigger variations than I_L. The current I_S depends on the recombination in the cell, meaning that V_{oc} measures this very recombination [OKA+16].

  In Fig. 1.1.5 we can see an I-V curve of a solar cell, and the product of the current and voltage which corresponds to the power output P for those specific operating conditions. From it stems an additional parameter that characterizes

the solar cell, the **maximum power point**, correspondent to the product $I_m \times V_m$, that is, when $\frac{d(IV)}{dV} = 0$. It is graphically given by the grey rectangle displayed in Fig. 1.1.5. The voltage V_m for the maximum power P_m obeys the following equation:

$$V_m = V_{oc} - \frac{kT}{e} \ln\left(1 + \frac{eV_m}{kT}\right) \tag{1.3}$$

At the maximum power point, the power output with strong sunlight (1 kW/m^2) shining on the cell is know as its 'peak power', and that is why photovoltaic systems are commonly rated in terms of their 'peak' watts (watt-peak, W_p) [WGWC07].

- **Fill factor (FF):** The ratio between the maximum power P_m and the product of the short circuit current I_{sc} with the open circuit voltage V_{oc}.

$$FF = \frac{V_m I_m}{V_{oc} I_{sc}} \tag{1.4}$$

It is used to evaluate the quality of the junction and measure the series resistance of the cell [WGWC07].

Another parameter used to evaluate a solar cell performance is the **efficiency**, η, which measures how efficient is the conversion of light to electrical power. It is calculated as the ratio between the maximum produced electrical power, $P_{\max}$ and the incident power, P_{in}.

$$\eta = \frac{P_{\max}}{P_{\text{in}}} = \frac{I_{sc} V_{oc} FF}{P_{\text{in}}} \tag{1.5}$$

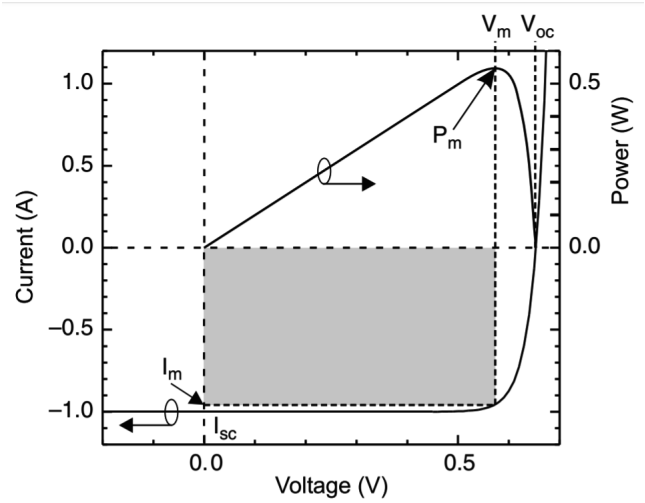

Fig. 1.1.5. I-V diagram (left and bottom axis) of a solar cell under illumination and extracted power (right axis). The grey rectangle is the maximum power region, with $P_m = I_m V_m$ (from [Gru10]).

1.1.2 Thin film solar cells

Nowadays, the most common material used for producing solar cells is silicon (Si), with crystalline silicon (c-Si) modules dominating the photovoltaic market with a share over 90% [ISE19]. As a result, they are the most extensively studied photovoltaic technology, with efficiencies surpassing 24% in the last years (Fig. 1.1.6) [ISE19], and an always decreasing cost in its components. However, silicon is an indirect (band gap) semiconductor, meaning that its absorption coefficient is very low, requiring a fairly thick cell to properly absorb all the sunlight and prevent it from simply passing through. This is not a problem for direct (band gap) semiconductors, which are able to absorb all sunlight with a few microns of thickness, that way potentially cutting down on the cost of materials [Gru10]. Despite this, the application of thin materials brings about additional costs.

The other main photovoltaic technology is based on direct semiconductors: Thin film solar cells, which have light absorbing layers considerably thinner than those of standard Si cells, currently holding around 4.5% of the global annual photovoltaics production [ISE19]. Thanks to their small-scale design and efficient semiconductor present in their cells, these are the lightest photovoltaic cells in the market, while still having significant durability. Compared to multicrystalline-Si (multi-Si) and

monocrystalline-Si (mono-Si) solar cells, these possess advantages like their flexibility, low weight and exceptional performance under conditions of low irradiation, high temperatures, and diffuse light, while also having the potential to require less amount of materials and energy to be manufactured [MGMAGC12][Pie04][Ber17]. The manufacturing of thin film modules is currently striving to increase along with the growth of the global PV market (Fig. 1.1.7 Left), however, the efficiencies of the modules still have not reached the desired competitive level and its productions costs need to decrease in order for it to be taken as a true alternative to Si-based solar cells. Thin film photovoltaic technologies cover cadmium-telluride (CdTe), amorphous silicon (a-Si) and copper indium gallium selenide (CIGS) modules.

CIGS solar cells are currently the thin film solar cell with the most potential, having already achieved record lab efficiencies for thin film technology of 23.35% [Hut09]. That has translated into an increase of its production in the last few years, contrary to what has been happening with the other thin film technologies, as can be seen in Fig. 1.1.7 Right. CIGS solar cells will be the photovoltaic technology covered in this work.

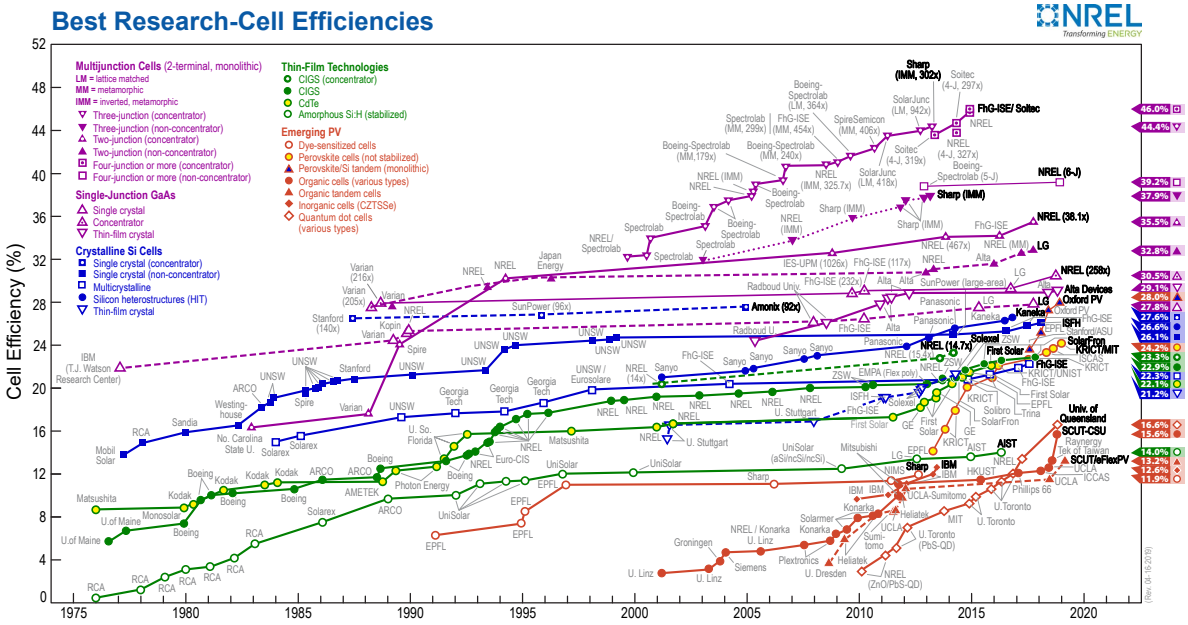

Fig. 1.1.6. Best research-cell efficiency chart for various photovoltaic technologies, plotted from 1976 to the present (from [NRE14]).

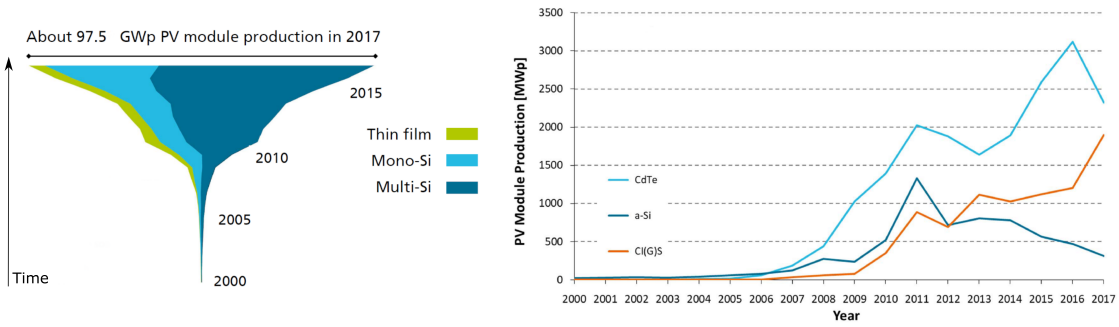

Fig. 1.1.7. Left: Annual global PV module production, in GWp. **Right:** Annual global thin film PV module production (from [ISE19]).

1.2 Development of CIGS thin film photovoltaics

1.2.1 CIGS solar cell

The photovoltaic technology based on thin films of CIGS saw its first developments in the 1970s, with the fabrication of the first cell based on a CdS/$CuInSe_2$(CIS) heterojunction, still with a low efficiency. Since then, the technology had several improvements, such as alloying with gallium (Ga) to obtain CIGS, replacing the thick CdS layer with a thinner one, and adding other layers to boost the efficiency of the cell [RS17].

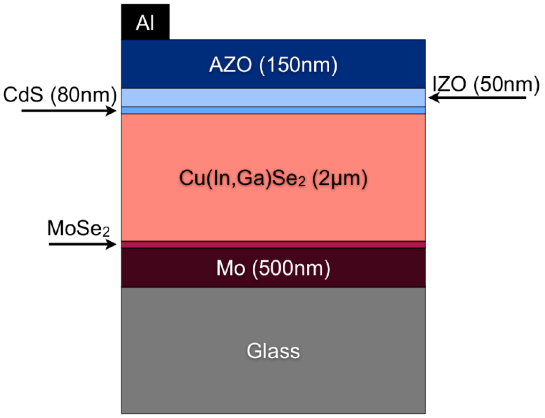

Fig. 1.2.1. Device structure of a standard CIGS solar cell. The thicknesses presented are approximate values that in reality are optimized for device performance [Bro11].

The device structure for the typical CIGS cell is drawn schematically in Fig 1.2.1, where the following layers can be seen:

- **Soda-lime glass (SLG):** The solar cell is grown on top of a substrate, usually a soda-lime glass, chosen to withstands the harsh conditions necessary to grow the absorber, like high temperatures and high vacuum, while also having a thermal expansion coefficient that is similar to that of the molybdenum (Mo) and CIGS layers [Sal11]. During growth, the sodium (Na) present in the glass diffuses into the CIGS film, improving device performance [Bro11]. Alternatively, a lighter and more flexible plastic (polyimide) film may be used instead of the soda-lime glass.

- **Mo back contact:** The main material used for the (positive) back contact in CIGS solar cells is molybdenum. This allows the layer to have low resistivity, endure the high temperatures necessary for growing CIGS, and it forms an ohmic contact with the CIGS. The choice of this material also allows for the Na to diffuse through this layer and into the CIGS film, and its reflectance in the visible spectrum is such that it allows some of the unused light (not absorbed in the first passage) to be reflected back to the absorber [Sal11]. Ideally, this reflectance could be higher, but a metal that is a better optical reflector while still having advantages for the back contact like those of the Mo has not been reported [OSW03][Sal11].

  During the CIGS deposition the Mo reacts with Se, forming an additional **$MoSe_2$ thin layer** [ABD+05] which has small benefits for the back contact of the cell, contributing to turning it into an ohmic contact, instead of a Schottky-type contact [WKNN01].

- **CIGS absorber:** A p-type CIGS absorber layer is grown on top of the back contact. CIGS is a I-III-VI_2 semiconductor material which crystallizes in a tetragonal chalcopyrite crystal structure. It is a solid solution of the copper indium selenide ($CuInSe_2$, or CIS) and copper gallium selenide ($CuGaSe_2$) compounds, with a chemical formula $CuIn_xGa_{1-x}Se_2$. CIGS has an exceptionally high absorption coefficient of around 10^{-5} cm^{-1} [Sal11], and its band-gap

depends on the fraction x of doping, which may vary from 0 ($CuGaSe_2$) to 1 ($CuInSe_2$), meaning that band-gap of CIGS varies between their respective band-gap values, that is, from 1.02 eV($CuInSe_2$) to 1.69 eV($CuGaSe_2$) [Sal11]. This means that by changing the Ga/(In+Ga) ratio, the performance of the cell can be enhanced [LES05]. The maximum device efficiencies are obtained in the CIGS band-gap range from 1.15 eV to 1.25 eV [CLB$^+$12].

The properties of CIGS are also related to the deposition technique used. The growing of a high quality CIGS absorber takes place with temperatures in the range 450 - 600 °C [RS17]. There are a number of methods for depositing CIGS, be it on rigid or in flexible substrates, depending on the criteria of the manufacturer regarding factors like film composition, reproducibility and cell efficiency, but these will not be detailed here.

It is worth pointing out that CIGS thin films often exhibit grain boundaries along its thickness, yet, apparently, these do not have a significant impact in the device performance [PZ03].

- **CdS buffer layer:** The cadmium sulfide (CdS) compound is a II - VI material which crystallizes in a wurzite structure. It is a n-type semiconductor with a direct band-gap energy of 2.42 eV (at room temperature) [EM03].

  The semiconductor cadmium sulfide has historically been used as the n-type buffer layer in the p-n heterojunction with CIGS. This layer is commonly deposited on top of the CIGS by chemical bath deposition (CBD). The use of CdS as the buffer layer has been subject to debate for a long time, since it offers both benefits and limitations.

  The CdS layer is able to electronically passivate the absorber surface, while at the same time having a protecting role on the absorber [SS11]. Also, since its refractive index is a value between those of ZnO and CIGS (Fig. 1.2.2), it successfully minimizes reflection, meaning it also has a role as an active optical element in the cell [ORN$^+$02].

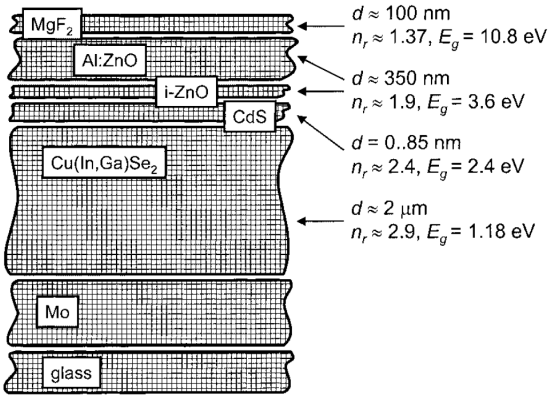

Fig. 1.2.2. Layer structure of a CIGS solar cell, showcasing the thickness d, refractive index n_r and band-gap E_g for different layers, according to [ORN+02].

However, the low band-gap of CdS limits the optimum performance of the cell, with the buffer layer having a lower collection efficiency that the absorber layer [Bro11]. Cadmium's toxicity also raises questions about the use of CdS. This has led to research of potential Cd-free buffer layers, such as In_2S_3, ZnS, ZnMgO and ZnSnO, with positive results, yet none of these have reached maturity for mass production as of this moment [NARA+10][LWH+13].

- **Intrinsic ZnO (IZO):** Prior to the deposition of the front contact, a thin layer of high resistivity zinc oxide (intrinsically doped ZnO) is grown on top of the buffer layer to prevent shunt paths[2] through the device due to the diffusion of aluminium (Al) from the layer of ZnO doped with Al (AZO) [RS17], providing a limiting effect of the conductance of the shunts (a passivation effect) thanks to its high resistivity [Ulf09]. The ZnO layer allows electron conduction through the conduction band [Mol16].

- **Al-doped ZnO (AZO):** A layer of ZnO is doped with Al to form a transparent conductive oxide layer, required to transport photo-generated electrons (current) to the metallic fingers on top the cell [Bro11][RS17], which acts as the front contact. An anti-reflective coating made of magnesium fluoride (MgF_2) may be added on top to reduce light reflection.

The IZO and AZO layers make up the cell window layer.

[2]Unwanted short circuit between the back and front surface contacts of a cell, that is, the electrodes.

1.2.2 Passivation with Al_2O_3

Since the properties of CIGS are closely related to its preparation, most of the research in the field has been focused on the improvement of its opto-electronic properties, rather than on developing new architectures [PKG+16]. Recently, research has also turned to improving the electrical performance of thin film solar cells by interface passivation, that is, by reduction of defects at the interfaces.

The use of aluminium oxide (Al_2O_3) in CIGS solar cells has been the subject of a number of works, particularly about its role as a passivation layer when deposited at the rear-surface of a CIGS solar cell. Its presence has shown to enhance the performance of the cell, without changing the CIGS structural properties [GLB+19].

Recently, the possibility of depositing insulator materials such as Al_2O_3, on CIGS, to be used as interface passivation layers, has been subject of study and characterization [CFH+18]. Apparently, the deposition of a Al_2O_3 layer by atomic layer deposition (ADL) does not seem to cause modifications to the surface of CIGS, and it is suggested that the with of the Al_2O_3 dielectric has an effect in the performance of the solar cell, presumably by a reduction of the concentration of defects. Although this passivation is believed to occur, the quantification and measurement of interface defects is still lacking. Currently, photoluminescence is the technique available to measure defects, but it is unable to separate contributions from the interface and from the bulk [SFL+14]. Muon spin spectroscopy offers an opportunity to better quantify and analyse these interface defects, and to measure the width of the defective region.

Chapter 2

State of the art

2.1 Muons as local probes of interface layers

2.1.1 Muon

The muon (μ) is an elementary particle which carries a positive (μ^+) or negative (μ^-) charge, for the case of the antimuon and muon respectively, and has spin 1/2, being classified as a charged lepton. Its main properties are summarized in Table 2.1.1. Muons are found in nature, being recognized mainly as the dominant particles of cosmic rays that constantly reach the surface of the earth, showcasing the effects of time-dilation in special relativity [Blu99]. However, these particular muons will not be the focus of this work, but rather the muon beams which are artificially produced in laboratory for use in condensed matter physics research.

	Muon
Mass	$m_\mu = 105.658$ MeV/c^2 $\approx 1/9 m_p$
Charge	$+e, (-e)$
Spin	$s = 1/2$
Magnetic moment	$\mu_\mu = 3.18 \mu_p$
Gyromagnetic ratio	$\gamma_\mu = 815.615$ MHz/T
Life time	$\tau_\mu = 2.19714$ μs

Table 2.1.1. Muon properties, with some extra remarks (from [Mor12]).

2.1.2 Production, decay and implantation in matter

In this type of research, artificially produced positive muons[1] are fired, and then implanted, in various types of matter with the intent of gaining knowledge about it. The implanted muons which actually end up in the sample, reside there for the remaining of their life without emerging again, working as probes in matter. These end up decaying into positrons which hold information about the muons from which they resulted.

The artificial production of muons requires high intensities, leading to the need of accelerators. In these, high energy proton beams are fired into a target (usually made of graphite). From this point the following steps occur:

High energy protons (500 MeV - 1 GeV [BM04]) interact with the protons of the nuclei in the target, producing pions according to the reaction:

$$p + p \rightarrow \pi^+ + p + n \tag{2.1}$$

Pions are unstable particles (lifetime of 26ns [NSD14]), and decay into muons and neutrinos (Fig. 2.1.1) according to:

$$\pi^+ \rightarrow \mu^+ + \nu_\mu \tag{2.2}$$

[1]From this point forward the positive muon will be referred to only as muon.

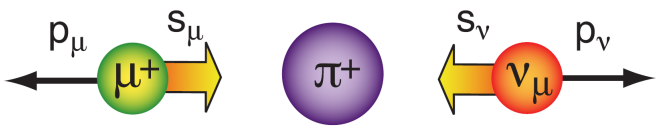

Fig. 2.1.1. Schematic of the pion (π^+) decay into a positively charged muon (μ^+) and a muon neutrino (ν_μ). With the pion at rest, the resulting muon ends up having 100% spin polarization at production (from [NSD14]).

The pions are produced at rest in the laboratory, which means that when they decay, in order for momentum to be conserved, the muon and neutrino must have equal and opposite momentum. Also, since the pion has zero spin, in order to conserve the total spin, the muon spin will be opposite to the neutrino spin, which itself is antiparallel to its momentum (it has negative helicity) since only left-handed neutrinos are produced in nature [Ama18][Blu99]. This implies that the muon spin is also antiparallel to its momentum. This allows the produced beam to have mainly 100% spin polarized muons.

The muon beam then produced, by extracting the muons decaying from pions at rest in the target, is directed to the samples, where the muons are implanted.

The magnetic moment of a muon interacts with local magnetic fields (moments, currents,...), with the muon polarization containing information about these static and dynamic local properties [Mor12]. The muons which stop in the matter decay after a period of time t with probability $\exp(-t/\tau_\mu)$ (where τ_μ is the muon's lifetime)[Blu99], resulting in the following three-body decay process:

$$\mu^+ \rightarrow e^+ + \nu_e + \bar{\nu}_\mu \tag{2.3}$$

In the muon decay there is also no conservation of parity. This leads to a propensity for positrons to be emitted along the direction of the muon spin when it decays. Thus, the direction of the emitted positrons will be dependent on the spin orientation of the decaying muon. A careful analysis of the asymmetry in the emission of the positrons provides the desired information regarding the interaction, over time, between the implanted muons and their surrounding environment in the sample.

2.1.3 Muon spin spectroscopy - μSR

A μSR experiment encompasses the previously referred mechanisms. The 100% polarized muons travel from the production target to the sample, directed in such a way that the spin polarization is maintained. When implanted in the sample, these have a kinetic energy of 4 MeV, yet it decreases to a few keV in a matter on nanoseconds due to ionization of atoms and scattering with electrons, followed by a series of electron capture and loss reactions which reduce the muon energy to a few hundred eV in just a hundreds of picoseconds [Blu99]. During this entire thermalization process the overall change in the spin direction of the muon is less than 15 mrad, therefore, it can be considered to be preserved [Nag03].

The three body process decay that happens afterwards leads to a distribution of positron energies, which results in a spatial emission distribution (Fig. 2.1.2) correlated with the orientation of the decaying muon's spin.

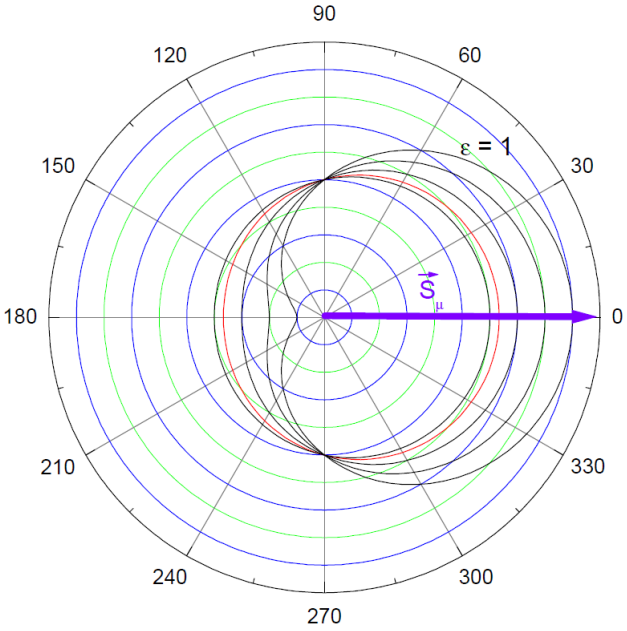

Fig. 2.1.2. Spatial emission distribution of decay positrons as a function of reduced positron energy, ε. The initial muon-spin direction is represented by the arrow (from [Vil07]).

The angular distribution of the emission of positrons with respect to the initial muon-spin direction, can be measured and can be monitored simply by a pair of

positron detectors placed opposite to each other around the sample. These are usually designated as forward (F) and backward (B) detector, as illustrated in Fig. 2.1.3.

By having a pair of detectors around the sample capable of detecting the positrons in opposite directions, it is possible to obtain information about the evolution of the spin of the muon over time through the function $A(t)$, that measures the asymmetry in the emission of positrons in the forward-backward direction:

$$A(t) \equiv A_0 P_0(t) = \frac{N_B(t) - \alpha N_F(t)}{N_B(t) + \alpha N_F(t)} \tag{2.4}$$

where N_B and N_F are the number of events recorded on the backward and forward detectors, respectively, and α is a parameter correcting possible imbalance of detectors due to geometry, sample position or detector efficiencies. Information about the interaction of the muon spin or magnetic moment with its local spin or magnetic environment is given by A_0, the experimentally observable maximum asymmetry, and $P_0(t)$, from which one can extract the physical information about the surrounding system [NSD14].

In the presence of a magnetic field B applied perpendicularly to the initial muon spin, the spin of an unbound muon that is implanted into a non magnetic sample precesses with angular frequency

$$\omega_\mu = \gamma_\mu B, \tag{2.5}$$

called the Larmor frequency, where the gyromagnetic ratio of the muon, γ_μ, is given by $\gamma_\mu = 2\pi \times 135.534(5)$ MHzT^{-1}. Local fields present in the sample may superimpose with the applied field, allowing to follow local magnetic phenomena as a function of an experimental parameter by measuring the time dependence of the muon polarization [NSD14].

The histogram in Fig. 2.1.4 (Left) shows the periodic maxima and minima observed when the spins of the muon are aligned with each detector. The asymmetry function 2.4 allows to extract the signal that translates the evolution of the muon spin polarization of the muons through time, seen in Fig. 2.1.4 (Right).

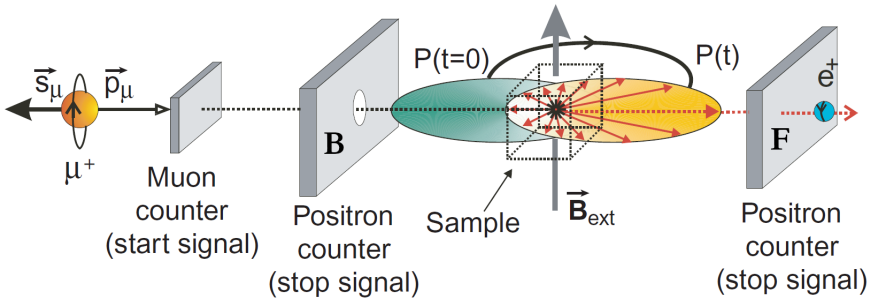

Fig. 2.1.3. Example of a detector configuration in a μSR experiment, with an externally applied transverse magnetic field. The backward and forward detectors are marked with the letters B and F, respectively (adapted from [BM04]).

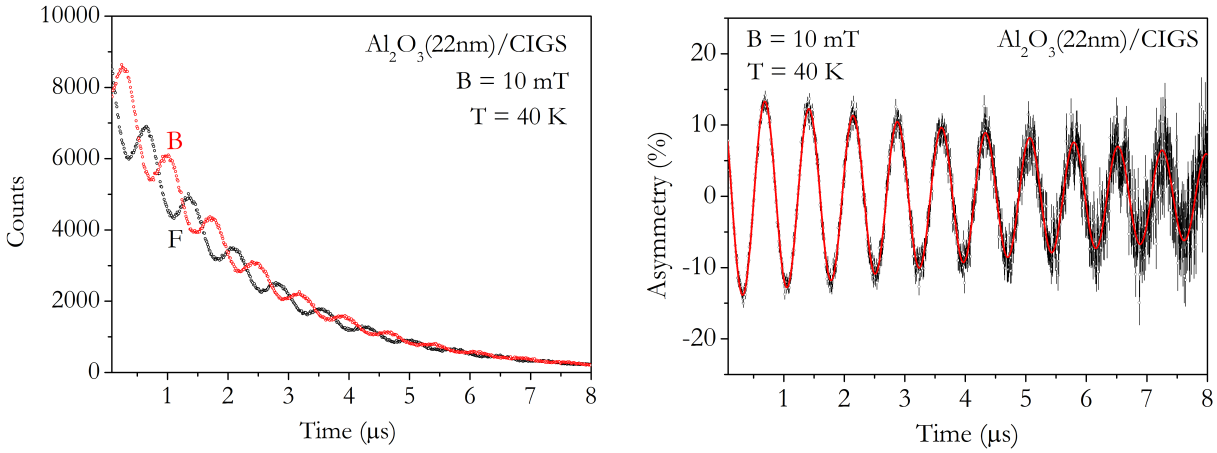

Fig. 2.1.4. Left: Histogram for the detection of positrons e^+ in the backward (B) and forward (F) detector, for one of the samples used in this work; **Right:** Asymmetry spectrum obtained from the raw detection histograms, for the same sample.

In the μSR technique the magnetic field may be applied perpendicularly to the initial muon polarization, or longitudinally, leading to different effects in the muon polarization. It is even possible to make studies without applying an external magnetic field, which may be useful for specific situations. The nature of the production source also has important implications on the characteristics of the experiments performed [NSD14][Blu99]. If it is a continuous muon beam (CW), represented in Fig. 2.1.5 (a), then the muons arrive at various intervals, one at a time, requiring precise high speed electronics to correctly register the arrival of muons and detection of positrons. This is hard, considering that the muon is a relatively long lived particle ($\tau_\mu = 2.2\mu s$). Muons arriving intermittently lead to a high background, meaning that

the time windows is small, but the time resolution is high, limiting lower frequencies but allowing work with high frequencies. A pulsed muon beam, represented in Fig. 2.1.5 (b), on the other hand, does not have to deal with this difficulty since it produces pulses with a large number of muons, making it unnecessary to detect when each muon arrives. Having this high number of muons arriving, a few background events are less significant, meaning that the background is low. This allows to have long time windows without statistical issues, but a small time resolution ($\sim 1/\tau_w$), limiting higher frequencies, due to the time width τ_w of the incoming muon pulse.

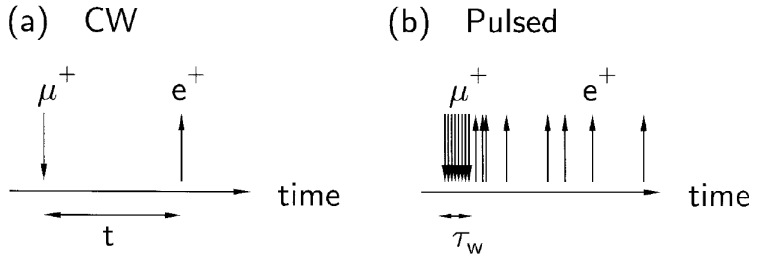

Fig. 2.1.5. Illustration of the two types of muon beam production sources. **(a)** Continuous wave; **(b)** Pulsed (from [Blu99]).

There are currently only 4 user facilities in the world prepared to carry out experiments involving muon beams. The Paul Scherrer Institute (PSI) in Switzerland and TRIUMF in Canada operate CW beams and ISIS in the UK and KEK in Japan operate pulsed beams (50 Hz) [Gug16]. The LEM instrument at PSI was used in this work.

2.1.4 Muon final states

Implanted muons can sometimes thermalize and pick up an electron, forming a neutral atomic state called muonium (Mu=μ^+e^-) analogue of the hydrogen atom, since it possesses similar reduced mass, Bohr radius and ionization energy. Its main properties are summarized in Table. 2.1.2.

	Muonium
Reduced mass	$\bar{M}_{\mathrm{Mu}} = 0.9956 \times \bar{M}_{\mathrm{H}} = 0.995\ (\mathrm{m}_e)$
Atomic radius (ground state)	$a_{\mathrm{Mu}} = 1.0044 \times a_0 = 0.532$ Å
Ionisation energy	$R_{\mathrm{Mu}} = 0.9956 \times R_y = 13.54$ eV

Table 2.1.2. Muonium properties, where $\bar{M}_{Mu}$ is its reduced mass, a_0 is the atomic radius and R_y is the Rydberg unit of energy, which corresponds to the ionisation energy of the hydrogen atom (from [Ama18][Vil07]).

The muon implantation may have several outcomes which are reproduced in Fig. 2.1.6. This figure represents the transition-state model proposed by Vilão et al. for dielectric oxides, in which incoming muon may or may not capture an electron when slowing down. By the end of the thermalization process the muonium may end up in one of three states: Interstitial muonium or atom-like muonium ($\mathrm{Mu}^0_{\mathrm{atom}}$), bound muonium ($\mathrm{Mu}^0_{\mathrm{bound}}$) and bound muon ($\mathrm{Mu}^+_{\mathrm{bound}}$). A muon which, by the end of the thermalization process, has not captured an electron (Mu^+), finds a stable space for its positive configuration at the anion-bound state ($\mathrm{Mu}^+_{\mathrm{bound}}$). If the muon captures an electron it ends up in the transition state, characterized by a weak hyperfine interaction and with a diamagnetic behaviour, and may then end up either in an oxygen-bound configuration (in the neutral state $\mathrm{Mu}^0_{\mathrm{bound}}$ or in the positively charged state $\mathrm{Mu}^+_{\mathrm{bound}}$) or in the relaxed interstitial configuration $\mathrm{Mu}^0_{\mathrm{atom}}$ [Alb17][Gue18][VVA+17].

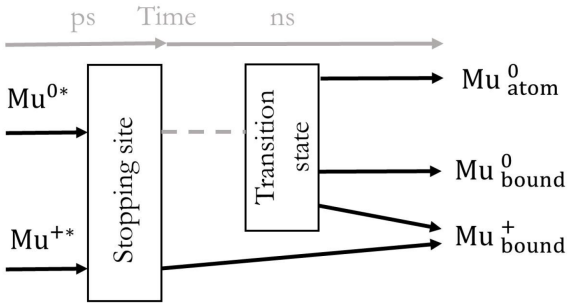

Fig. 2.1.6. Possible outcome of a muon implantation. Positive muons which do not couple with a electron are immediately bound to the lattice, but muonium which goes through the transition state can reach different configurations. The * marks the muons that end up resting at an interstitial site in the unrelaxed lattice (from [Alb17]).

The muonium can be distinguished by the hyperfine interaction that couples the

muon spin and electron spin, which is described, in the simplest case, by an isotropic Fermi contact interaction between the muon spin $\vec{S}_\mu$ and the electron spin $\vec{S}_e$, with the hyperfine hamiltonian given by:

$$H = hA\vec{S}_\mu \cdot \vec{S}_e \tag{2.6}$$

where A is the hyperfine interaction [Gue18]:

$$A = \frac{\omega_0}{2\pi} = -\frac{2}{3\pi}\mu_0 g_\mu \mu_\mu g_e \mu_B |\Psi(r=0)|^2 \tag{2.7}$$

where ω_0 is the angular frequency of the Fermi contact interaction, g_μ and g_e are the gyromagnetic factor of the muon and electron respectively, $\mu_{mu} = \frac{e\hbar}{2m_\mu}$ and $\mu B = \frac{e\hbar}{2m_e}$ are the muon and Bohr magneton respectively and $|\Psi(r=0)|^2$ is the electron density at the muon. The hyperfine interaction constant for muonium in vacuum is A=4.4633 GHz [LBD$^+$99].

In the presence of the magnetic field B typically present in μSR experiments, two additional terms referring to the muon and electron Zeeman terms must be added to the hamiltonian:

$$H = hA\vec{S}_\mu \cdot \vec{S}_e - M_\mu \cdot \vec{B} - M_e \cdot \vec{B} \tag{2.8}$$

where M_μ and M_e are the muon and electron magnetic moment operators.

As an example, a typical muonium signal for beryllium oxide (BeO), from [MVV$^+$17], can be seen in Fig. 2.1.7. Here we can observe that for different magnetic fields both the line correspondent to the diamagnetic state (ν_d) and the lines correspondent to a muonium state (ν_{12}) and (ν_{34}) vary both in frequency and amplitude.

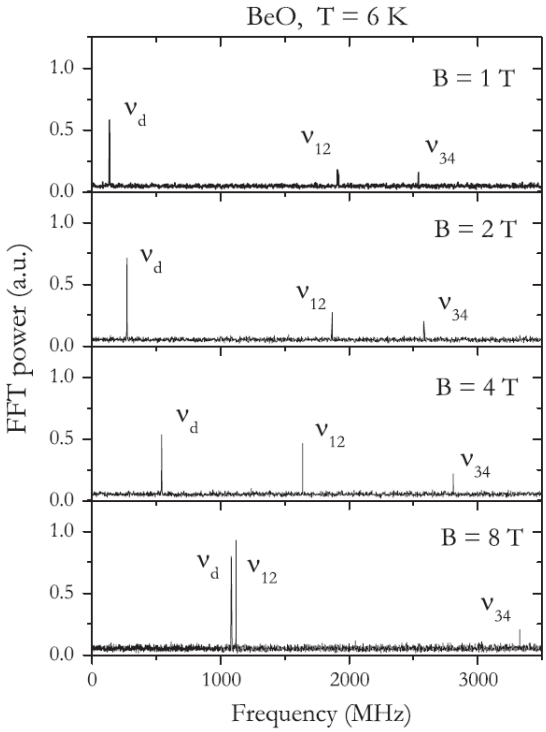

Fig. 2.1.7. Fast fourier transform (FFT) of μSR spectra obtained with fields of B = 1 T, B = 2 T, B = 4 T and B = 8 T, at T = 6 K, for beryllium oxide (BeO) (from [MVV$^+$17]).

The resolved muonium lines in BeO are frequently inaccessible due to dynamical processes that lead to depolarization of the fraction of polarization due to muonium. The corresponding polarization is then washed out and becomes invisible, except for its impact on the maximum observable asymmetry. These depolarized fractions are hence usually known as missing fractions.

2.1.5 Low Energy Muon Beam (LEM)

The usual μSR experiments have the hindrance of not being able to study thin samples, due to the deep implantantion that comes with an implantantion energy in the order of the MeV, and also because the stopping range of the muon itself extends over a certain distance (for E = 4.1 MeV it can go from 0.1 to 1 mm) [BM04]. Nowadays the scope of μSR experiments is not limited to bulk investigations, being also possible the study of thin films, multi-layer surfaces, and regions close to the surface. Having the means to successfully probe these structures is very much important since their

reduced dimensionality and the contact between the interfaces results in a different behaviour from that of bulk materials. This is done by "slowing down" the muons, that is, by producing muons with low energies, in the range of keV, that are able to penetrate a material on the nanometre length scale. Generally, muons with energies below 100 keV are called "slow muons", with the term "very slow muons" or "epithermal muons" being used for muons with energies between 1 - 50 eV. For energies lower than that the muons are considered as "ultraslow muons" [BM04].

Fig. 2.1.8. The LEM spectrometer at the PSI facility in Switzerland (photo from the author).

This is achieved only at the Low-Energy Muon Facility (LEM) in PSI, where it is possible to have a quasi-continuous beam of 100% polarized muons, with tunable energies ranging from 0.5 to 30 keV, a time spread around 5 ns and intensities of around 1000 muons/s [NSD14][Mor09]. The LEM consists of two instruments:

- The source of the low-energy muon beam and its transport system (the $\mu E4$ surface muon beam line, the cryogenic moderator and system of electrostatic elements to aid in the transport of muons).
- The low-energy μSR spectrometer (LE-μSR), visible in Fig. 2.1.8.

Table 2.1.3 showcases the main characteristics of the LEM instrument, also regarding the $\mu E4$ beam line [PMD$^+$05], which is the large acceptance beam line for muons with low momentum used for the LEM facility.

Momentum of $\mu E4$ beam	27.7 MeV/c
Momentum(energy) of low-energy muon beam	0.45 - 2.5 MeV/c (1 - 30 keV)
Mean range of low-energy muon beam	10 - 200 nm
$\mu E4$ muon beam polarization	>90%
Low-energy muon beam polarization	>90%
Direction of muon spin at sample	-90° - +90° (+90° is in beam direction)
Positron detectors' positions	4 downstream - Left/Top/Right/Bottom 4 upstream - Left/Top/Right/Bottom

Table 2.1.3. General specifications of the LEM facility (from [PSI26]). Note that the positions of the positron detectors are given with respect to muon momentum.

The method used at PSI to produce low energy muons is the use of a specific material (moderator) in which particles are implanted, where their interactions lead preferentially to an emission at energies of a few eV (a reduced and limited energy spectrum), effectively slowing them down. The production of this beam is thus accomplished by moderating a surface muon beam with fully polarized muons and an initial energy of about 4 MeV to a beam of low energy (1 - 30 keV) in which the muons retain the 100% polarization.

A moderator is able to efficiently convert energy particles into thermal or epithermal (a few keV) particles. The moderation is done by passing the 4 MeV surface muon beam through a moderator consisting of a thin layer (of a few hundred nm) of a van der Waals bound solid rare gas, or solid nitrogen films, deposited on a cooled down (to ∼10K) substract with good conductivity at low temperatures. The entire process occurs in a ultra-high vacuum regime in order to maximize the efficiency of the moderation. Only a small fraction of the initial muons produce very slow muons with a mean energy of 15 eV. When exiting the moderator, using a electrostatic transport system , with the moderator set to high voltages of up to +20 kV, the very slow muons are accelerated to a maximum energy of 20 keV (low energy muons) with a small spread of 20 eV, and then are separated from the major fraction of outcoming "fast" (degraded, not moderated) muons which possess a mean energy of about 500 keV. This separation is possible by identifying their distinct time-of-flight (TOF)

between the start scintillator and the trigger detector of the system [PSI31b][PSI31a].

In order to optimize the transport system settings, a sample cryostat or a sample heater is placed at the sample position, at the end of the transport system. The temperature range currently covers 2.5 - 570 K. The magnetic field applied to the sample surface may be done so longitudinally, transversely or it may be zero. The sample is mounted on the cryostat, electrically insulated, so that an acceleration or deceleration high voltage of up to ±12 kV may be applied to it. This makes it possible to have low energy muons in the energy range 1 - 30 keV. The positrons from the muon decay are then detected by scintillator segments around the vacuum tube, with the readout being achieved by avalanche photo detectors [PSI31b][PSI31a][BM04]. The setup is schematized in Fig. 2.1.9, with some technical remarks.

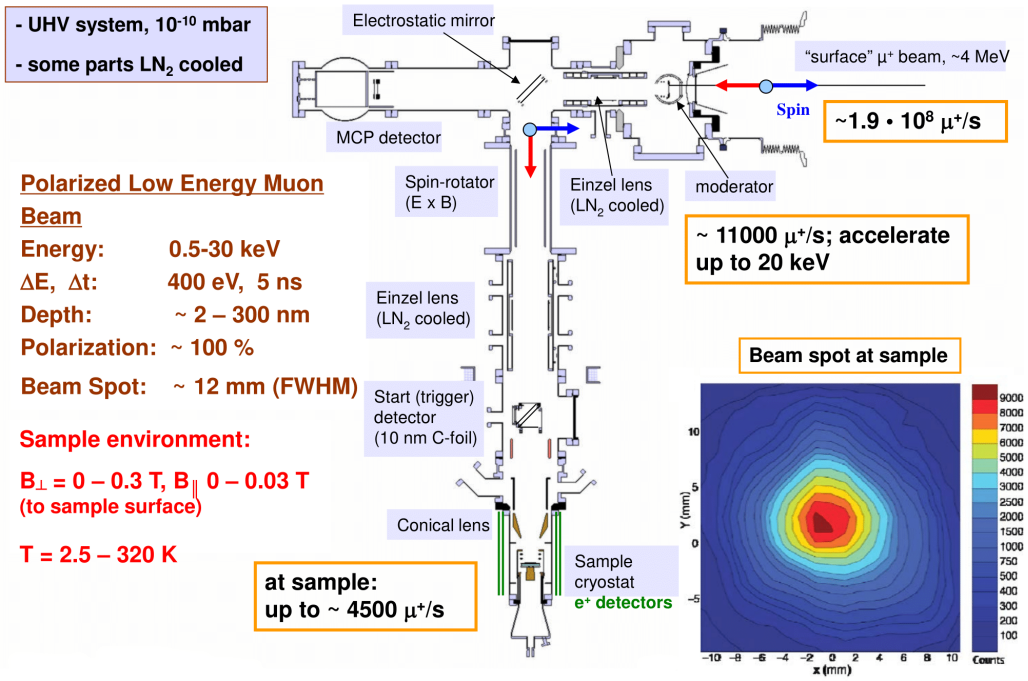

Fig. 2.1.9. Setup and characteristics of the LEM instrument at the PSI facility in Switzerland (from [Mor14]).

2.2 μSR for study of CIGS interfaces

2.2.1 State of the art

The μSR has proved to be a successful technique to study the interface properties of complex semiconductors [AVV+18], by using slow (low energy) muons (mentioned in section 2.1.5) as probes of the defect layer at the surface or interface of these materials. The fact that the muon beam has adjustable energy values in the range 1 - 30 keV, makes it possible to vary the depth of implantation of these muons in the nanometre range, as can be observed in Fig. 2.2.1 for a structure with Cu(In,Ga)Se_2 (CIGS) as the p-type absorber and CdS as the buffer layer. This technique will be used in this work to obtain information about the passivation of CIGS surfaces with the dielectric oxide Al_2O_3.

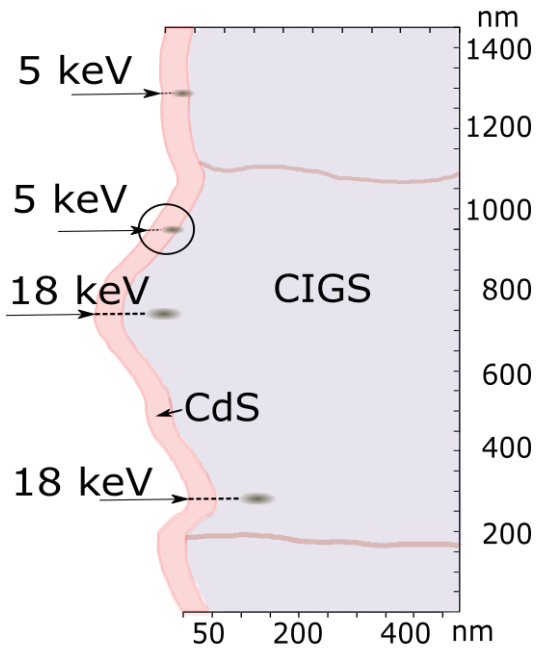

Fig. 2.2.1. Representation of the different implantation depths achieved with different muon implantation energies.

2.2.2 Past experiments

In a previous study [AVV+18], this slow muon technique was used to study p-n junctions for solar cells. Two different materials used in solar cells were studied: Cu(In,Ga)Se_2 (CIGS) and Cu_2ZnSnS_4 (CZTS), which have similar structures. Two different buffer layers were also considered, namely CdS and a Cd-free material, ZnSnO. These experiments were performed in the LEM facility, at PSI.

In this experiment positive muons were implanted with energies ranging from 2 to 25 keV, in a magnetic field (B = 10 mT) with transverse field configuration, and with temperatures ranging from 5 to 300 K. The variation of the muon implantation energy worked as a mean to make a depth-dependent study of the films. The relation between the energy of the muon beam and the stopping range of the muons was calculated for these materials using the Monte Carlo code TRIM.SP, as illustrated in Fig. 2.2.2.

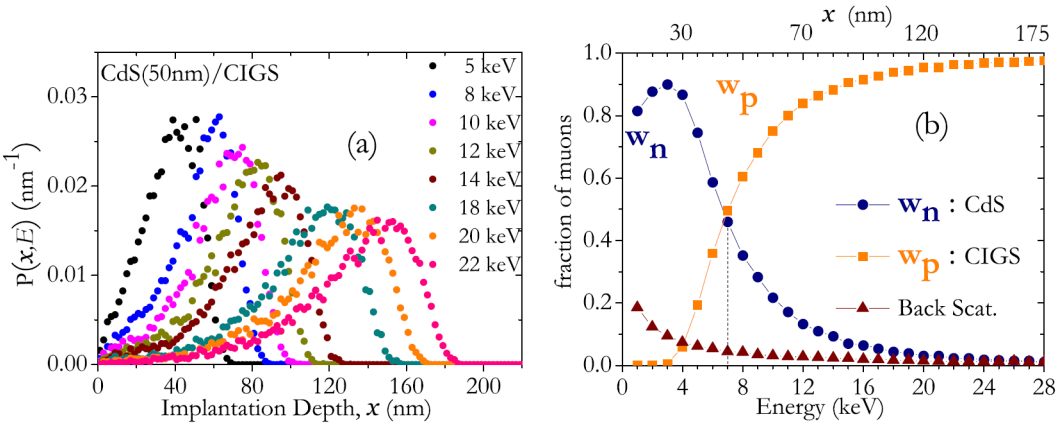

Fig. 2.2.2. Data obtained from the Monte Carlo code. **a)** Muon stopping probability per unit length, $P(x, E)$, as a function of implantation depth for different implantation energies. **b)** Relative weight of muons stopping on the n-type and on the p-type layers, ω_n and ω_p respectively, as a function of implantation energy (from [AVV+18]).

The probability that a muon with implantation energy E stops between two depths, a and b, that is, in the range $a < x < b$, can be calculated by numerical integration of the muon stopping probability per unit length, $P(x, E)$, obtained from the Monte Carlo simulation:

$$P(a,b,E) = \int_a^b P(x,E)dx \tag{2.9}$$

The diamagnetic fraction as a function of the muon implantation energy, together with the relative weight of muons stopping on the n-type and p-type layers, ω_n and ω_p, obtained in the Monte Carlo simulations, allowed to calculate the expected diamagnetic fraction:

$$f_{dia}^{pred}(x) = \omega_n(x) f_{dia}^n + \omega_p(x) f_{dia}^p \tag{2.10}$$

where f_{dia}^n and f_{dia}^p are the characteristic values for the n-type and p-type materials, respectively.

In Fig. 2.2.3 (a) the variation of the diamagnetic fraction $\Delta f = f_{dia} - f_{dia}^{pred}$ is represented as a function of the average implantation depth. A way to model the drop visible in the graphs is by assuming that the physical origin of this drop is described by a function $Y(x)$ with a square well shape, as can be seen in Fig. 2.2.3 (b).

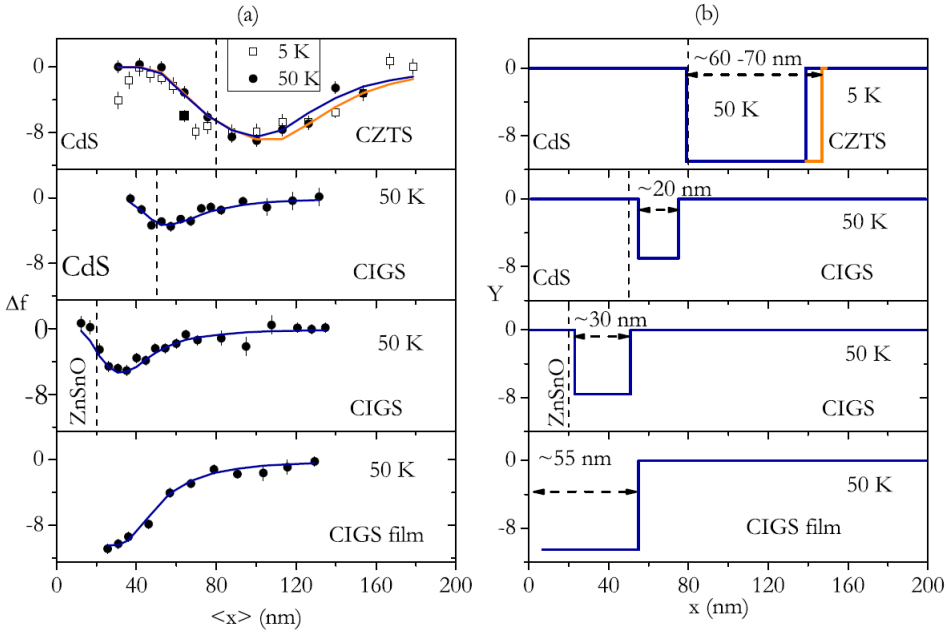

Fig. 2.2.3. a) Variation of the diamagnetic fraction Δf as a function of the average implantation depth $\langle x \rangle$ for four different configurations. **b)** Expected function if the cause of the effect is assumed to be a function $Y(x)$, which has a square well shape. The dashed vertical lines represent the position of the material's interface (from [AVV+18]).

This square well approach means that Y=0, except in the interval $a < x < b$:

$$Y(x) = -C, \qquad a < x < b \tag{2.11}$$

where C, a and b are adjustable parameters corresponding to the depth (minimum value of the function), beginning and end of the square well. Therefore, the curves in (a) are non-zero in the same interval:

$$\Delta f = -C \times P(a, b, E), \qquad a < x < b \tag{2.12}$$

From this analysis it can be observed that, in the case of the junctions, the dip effect (decrease of the formation probability of bound muonium - Mu_{bound}) occurs at the p-n interface, more specifically in the side of the absorber, while in the film it happens at the surface.

From the observation of this change in the diamagnetic fraction, two mechanisms were proposed, both related to Mu^{0*}_{atom} (muons formed directly at an interstitial position in the unrelaxed lattice):

Space charge region (SCR) model. In this model, the muon is sensitive to the net charge from the SCR, located in the absorber.

The changes in the missing and diamagnetic fractions depend, according to this model, on the outcome of the muonium at the interstitial position. This outcome can be one of two, depending if it stays neutral:

$$Mu^{0*}_{atom} \rightarrow Mu^{0}_{atom} \tag{2.13}$$

or if it captures a hole:

$$Mu^{0*}_{atom} + h^{+} \rightarrow Mu^{+}_{atom} \tag{2.14}$$

The first reaction is related to the missing fraction, while the second is related to the diamagnetic fraction. As a consequence, for a given material and temperature, the diamagnetic fraction becomes a function of the concentration of holes. The concentration of holes is reduced in the SCR, so in this model the

width of the dip corresponds to the width of the SCR. Ultimately though, the expected width of the SCR for the junctions is inferior to the width where the dip of diamagnetic fraction was observed, meaning that this dip cannot be a measure of the SCR width of the materials.

Surface defect layer (SDL) model. In this model, the muon if sensitive to defect-rich and disordered regions like the SDL, which is located within the absorber, near the interface.

In this case, the changes in the missing and diamagnetic fraction depend on which of the following two processes is dominant:

$$Mu^{0*}_{atom} \rightarrow Mu^{0}_{atom} \tag{2.15}$$

$$Mu^{0*}_{atom} \rightarrow Mu^{0/+}_{bound} \tag{2.16}$$

The first reaction is related to the missing fraction, while the second is related to the diamagnetic fraction. According to this model, the dip in diamagnetic fraction near the p-n interface, and near the surface in the case of the film, is the result of the presence of defects and structural disorder in the materials, which control the extent of reaction 2.16. In this case, both the depth and width of the dip predicted for these materials seem to be consistent with the experimental values.

From the analysis, the main conclusion is that the dip observed near the buffer-absorber interface and in the surface of the CIGS film is a result of processes occurring in the surface defect layer. This suggests that the μSR technique is a valuable tool for studying the surface defect layer in heterostructures or film surfaces.

2.2.3 The need for a general tool for depth-resolved information

The procedure used in the article presented in section 2.2.2 was useful for drawing conclusions, yet it was not optimized and was limited to a single μSR parameter (the

diamagnetic fraction). The parameters in the square well were determined manually and the method itself should be changed in order to be applied to any μSR parameter. A more general and optimized tool is needed to obtain depth-resolved information from the implantation energy dependence of the experimental parameters in a LEM experiment, in a systematic way. Such method would be useful not only for the current work, but also for future projects in the scientific community that involve any type of interface in a LEM experiment.

The development of this method became the central goal of this thesis.

Chapter 3

Results and discussion

3.1 Overview

In order to study the effect that a dieletric layer has in a CIGS cell, four samples were supplied to our group, and taken to PSI to be studied in the LEM instrument.

The samples were grown and characterized by International Iberian Nanotechnology Laboratory (INL) personnel, with the growing taking place at the Uppsala University in Sweden just before the LEM run. These were kept in vacuum during the transport and while already in the PSI, avoiding oxidation, in order for the samples to maintain their original properties.

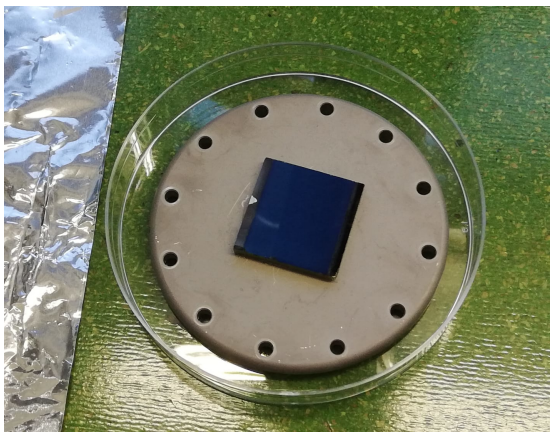

Fig. 3.1.1. One of the samples analysed at the PSI (photo from the author).

All samples used the same CIGS semiconductor substrate. These consisted of two samples of CIGS with a film of Al_2O_3 deposited on top, but with different Al_2O_3

thicknesses, a sample with CdS grown on top of the sample with the thinner layer of Al_2O_3, and a sample of CdS on top of the CIGS, without the dielectric layer in between. The Al_2O_3 was deposited using state-of-the-art atomic layer deposition (ALD), while the CdS was deposited using chemical bath deposition (CBD). This means that the interfaces and surfaces of these samples have different characteristics, with the chemical bath deposition leading to smoother interfaces, but with a chance of small aggregates in a scale of μm existing on the surface of the sample.

At first, the analysis of the LEM experiment data was done taking into account the growing parameters that control the interface widths of the samples. However, an accurate analysis requires precise values for the layer widths and associated errors. With this intent, a transmission electron microscopy (TEM) analysis was performed in INL by Marco Alberto [CAS+19] which yields the following values for the widths of the upper layers:

- Al_2O_3(22.0±3.5nm)/CIGS
- Al_2O_3(3.8±0.3nm)/CIGS
- CdS(59.2±2.3nm)/CIGS
- CdS(46.6±4.6nm)/Al_2O_3(4.3±0.2nm)/CIGS

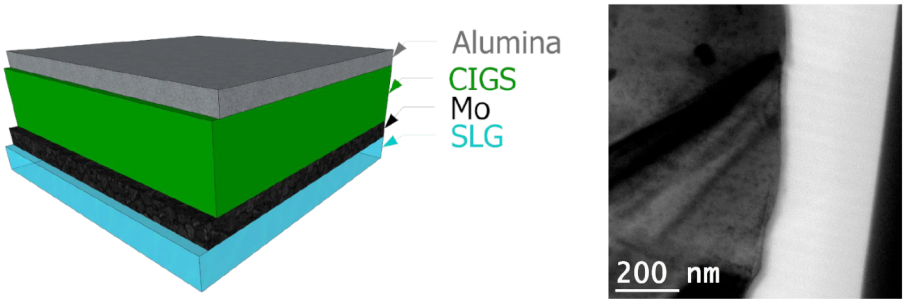

Fig. 3.1.2. Left: Al_2O_3 deposited through ALD, with an expected thickness of 25 nm. **Right:** Morphological characterization of the Al_2O_3(22nm)/CIGS sample, obtained through TEM analysis (from [CAS+19]).

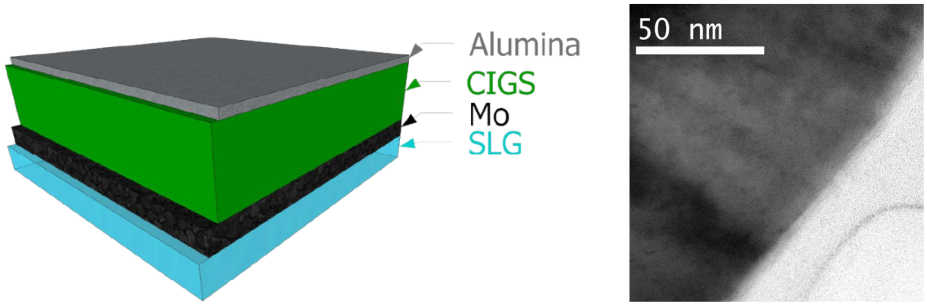

Fig. 3.1.3. Left: Al_2O_3 deposited through ALD, with an expected thickness of 5 nm. **Right:** Morphological characterization of the Al_2O_3(4nm)/CIGS sample, obtained through TEM analysis (from [CAS+19]).

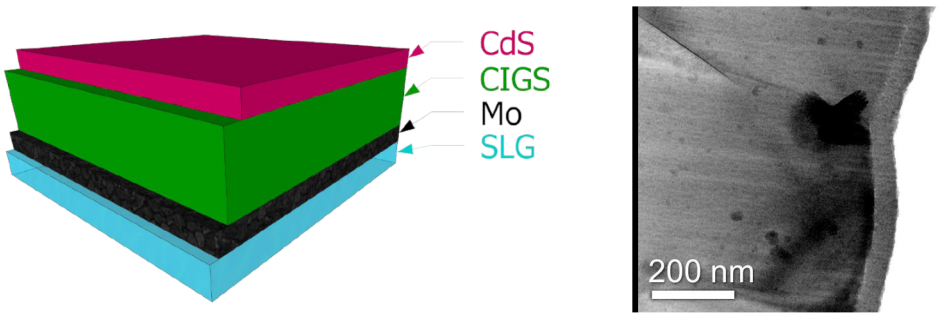

Fig. 3.1.4. Left: CdS deposited through CBD, with an expected thickness of 70 nm. **Right:** Morphological characterization of the CdS(59nm)/CIGS sample, obtained through TEM analysis (from [CAS+19]).

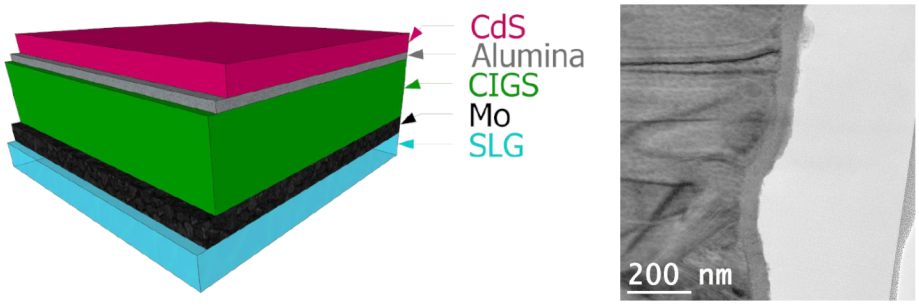

Fig. 3.1.5. Left: Al_2O_3/CdS deposited through ALD and CBD, with an expected thickness of 5 nm and 70 nm, respectively. **Right:** Morphological characterization of the CdS(47nm)/Al_2O_3(4nm)/CIGS sample, obtained through TEM analysis (from [CAS+19]).

The LEM instrument follows the operational process described in section 2.1.5. Each sample was mounted in the cryostat under argon flux, and then kept in vacuum.

3.2 Data treatment

The data obtained in the various LEM runs with different conditions, that is, the raw data, was analysed with the WiMDA program [Pra00], which is a muon data analysis program that is compatible with the muon data from the major μSR user facilities.

During the acquisition period, preliminary temperature dependent runs were performed using the Al_2O_3(22nm)/CIGS sample, from 20 to 200 K and with a constant implantation energy (E = 4.98 keV). The aim was to determine the observable diamagnetic fraction in the film and optimize the signal for subsequent measurements by determining the optimal temperature for the remaining acquisitions, performed with varying muon implantation energy E.

The analysis of this preliminary data was done considering 2 signal components with a Gaussian and Lorentzian relaxations (Fig. 3.2.1). The higher relaxations values were observed in the range of temperatures 30 - 50 K. In addition, energy dependent data from an Al_2O_3 single crystal (MTI 0001/1120) that was measured at ISIS in August/2010 (RB1010365 EMU flypast) was reanalysed in order to observe the relaxations and its temperature dependence. The depolarization rate for the fast and slow components of the signal in the Al_2O_3 single crystal can be observed in Fig. 3.2.2.

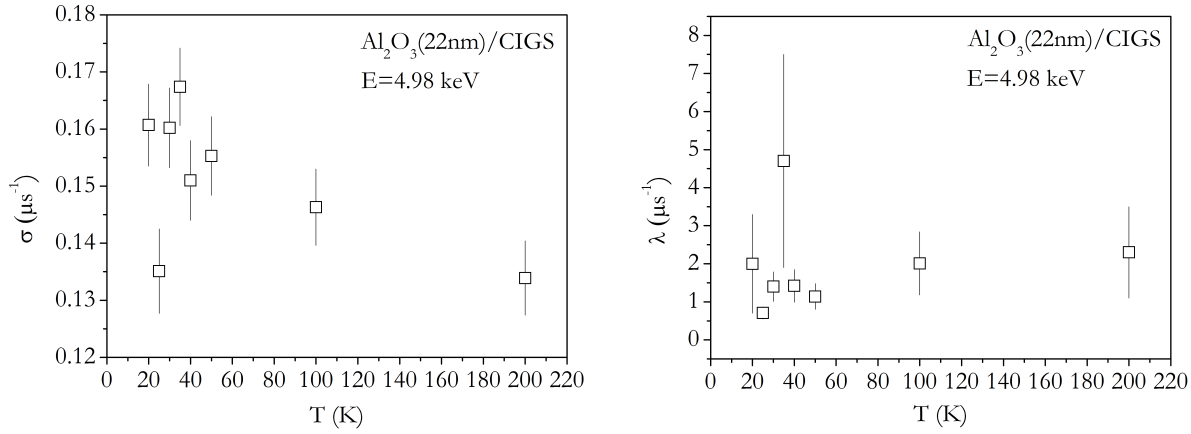

Fig. 3.2.1. Temperature dependence of the depolarization rates, σ and λ, for the Gaussian (**Left**) and Lorentzian (**Right**) relaxations, for the Al_2O_3(22nm) /CIGS sample used in this work.

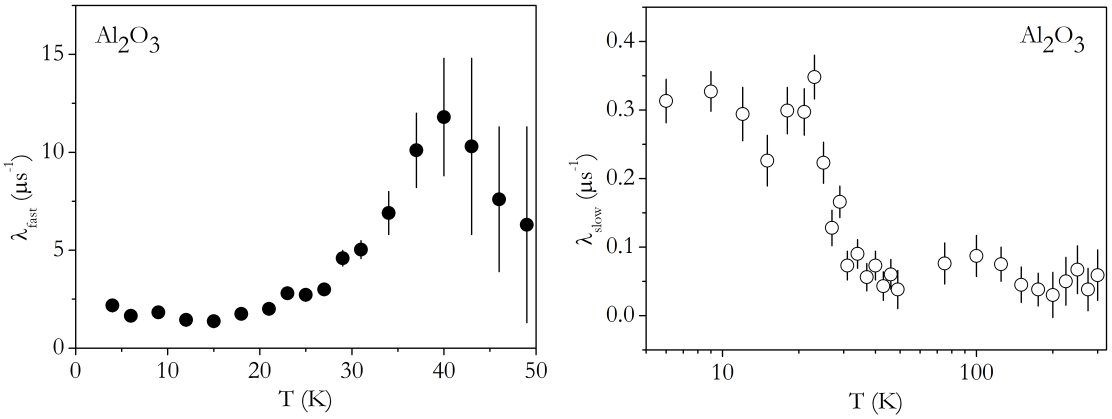

Fig. 3.2.2. Temperature dependence of the depolarization rates for the fast component (**Left**) and slow component (**Right**) of the signal relaxation for the Al_2O_3 single crystal.

The peak in relaxation observed in Fig. 3.2.2 happens for T = 40 K, which is also the peak in fraction of muonium. In the film a peak in the Gaussian relaxation is also observed at this temperature (Fig. 3.2.1 Left). Therefore, the temperature used in the succeeding runs was chosen to be T=40 K.

For the remaining of the experiment, detailed energy scans were performed for each sample at T = 40 K, in the presence of a transverse magnetic field of 10 mT, and using implantation energies ranging from 3 to 22 keV.

For all the samples, it was concluded that the data was best described by a Lorentzian-damped cosine at an angular frequency which is close to the Larmor frequency. This signal, represented by a time spectra like that of Fig. 3.2.3, corresponds to muons forming a state in the lattice with no net atomic magnetic moment, that is, a diamagnetic state. Therefore, the data was fitted with a function of the form:

$$A(t) = A_{dia} e^{-\lambda t} \cos(\omega t + \phi) \tag{3.1}$$

where A_{dia} is the diamagnetic signal amplitude, λ is the Lorentzian depolarization rate, ω is the signal angular frequency and ϕ is the phase. This is because even though CIGS data is usually fitted using a Gaussian damping [GAV$^+$00][VAG$^+$03][GAD$^+$03] [AVG$^+$14] [AVV$^+$18], the adequate relaxation function for Al_2O_3 is a Lorentzian. The Lorenztian was chosen since it is the best compromise to describe the full set of data.

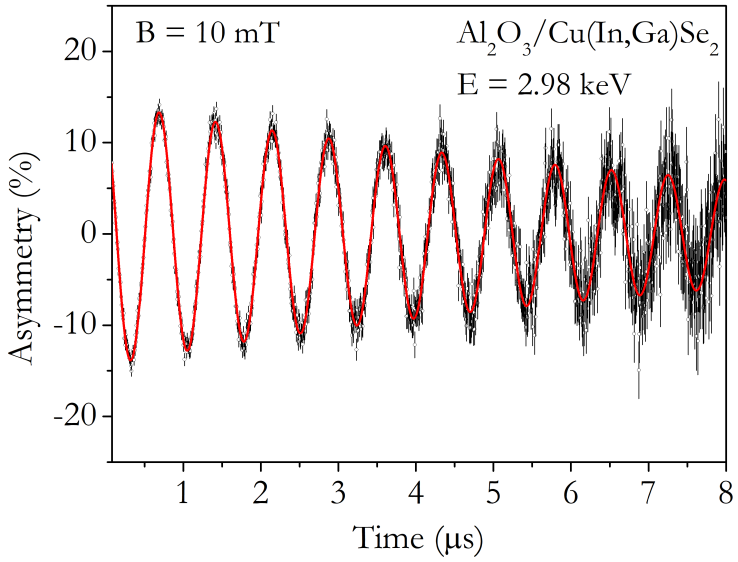

Fig. 3.2.3. μSR time spectrum in a Al_2O_3 in a Al_2O_3/Cu(In,Ga)Se_2 sample at T = 40 K, in the presence of a transverse magnetic field (B = 10 mT), for a muon implantation energy E = 3 keV. The red line is the calculated fit to the data using a Lorentzian-damped cosine function.

The WiMDA analysis was performed considering the time interval 0.08 - 8 μs. The data for a time lower than 0.08 μs displayed data points for which the muons decay in flight and should not be considered, while the data for time higher than 8 μs had large error bars and for that reason was also not accounted for. From the analysis we obtained information about parameters like the magnetic field, phase, asymmetry and relaxation, as a function of muon implantation energy. In the samples the amplitude of the visible μSR signal was always smaller than the expected maximum asymmetry, obtained by a silver calibration at 200 K and under a transverse field B = 10 mT, provided by Dr. Thomas Prokscha. This means that part of the μSR signal is missing, a situation that often occurs in materials for which the muons have strong interactions during their implantation stage [Cox09][VVA$^+$17][VVA$^+$18][VAGW19]. The parameter A_{dia} from the formula 3.1 was converted to the corresponding fraction of the total μSR sinal, f_{dia}, using a silver calibration and a sample size correction. The silver calibration curves obtained by the LEM team allow the correction for the change in maximum asymmetry with implantation energy for a given moderator voltage. Those calibration curves are described by the following expression:

$$A(E, \mathrm{Ag}) = p_0 \times [1 - \exp(-x/E_0) + p_1] \tag{3.2}$$

where $E_0 = 3.968$ is fixed.

In addition, it is also necessary to correct for the contribution of muons stopping outside the sample. This is obtained from measurements in a Ni plate (magnetic), and is given by:

$$A(E, \mathrm{Ni}) = A_0 \times \exp(-x/E_1) + \mathrm{offSet} \tag{3.3}$$

Most of the data was acquired using a moderator voltage of 15 kV, in which case the parameters provided by the LEM team are $p_0 = 0.0863(58)$, $p_1 = 0.1432(51)$, $A0 = 100(14)$, $E_1 = 1.83(22)$ and offSet $= 0.0095(10)$.

Thus, the final corrected diamagnetic fraction is simply the ratio of the sample asymmetry and of the Ag asymmetry (after removing the background asymmetry obtained in Ni measurements).

$$f_{\mathrm{dia}} = \frac{A(E, \mathrm{sample}) - A(E, \mathrm{Ni})}{A(E, \mathrm{Ag}) - A(E, \mathrm{Ni})} \tag{3.4}$$

For implantation energies of 17 - 22 keV the moderator voltage was 18 kV, for which the correction parameters are not known. We have therefore used the same correction as for a moderator voltage of 15 kV. In order to improve the correction, measurements were made for the CdS(46nm)/Al_2O_3(4nm)/CIGS sample with an implantation energy of 16 keV both with a moderator voltage of 15 kV and 18 kV. From these, a ratio of corrected asymmetries was obtained, and consequently used as a correction factor for the rest of the data analysis:

$$A(18\ \mathrm{kV}) = 1.02324 \times A(15\ \mathrm{kV}) \tag{3.5}$$

3.3 Development of a depth-resolved analysis

3.3.1 Basic analysis - Al_2O_3(22nm)/CIGS

As mentioned in section 3.2, the μSR signal in a Al_2O_3(22nm)/CIGS sample has a single component, meaning that we have only four experimental parameters: diamagnetic fraction, f_{dia}, muon spin relaxation rate, λ, spin precession angular frequency, ω, and initial phase ϕ. As already mentioned in section 2.1.3, the effective magnetic field at the muon position, B_{eff}, can be calculated from the spin precession angular frequency ω, $B_{\text{eff}} = \omega/\gamma_\mu$, where $\gamma_\mu/2\pi = 1.355 \times 10^8$ Hz/T is the muon gyromagnetic ratio.

After doing the WiMDA analysis for the Al_2O_3(22nm)/CIGS as a function of muon implantation energy, the following results were obtained for the different μSR parameters:

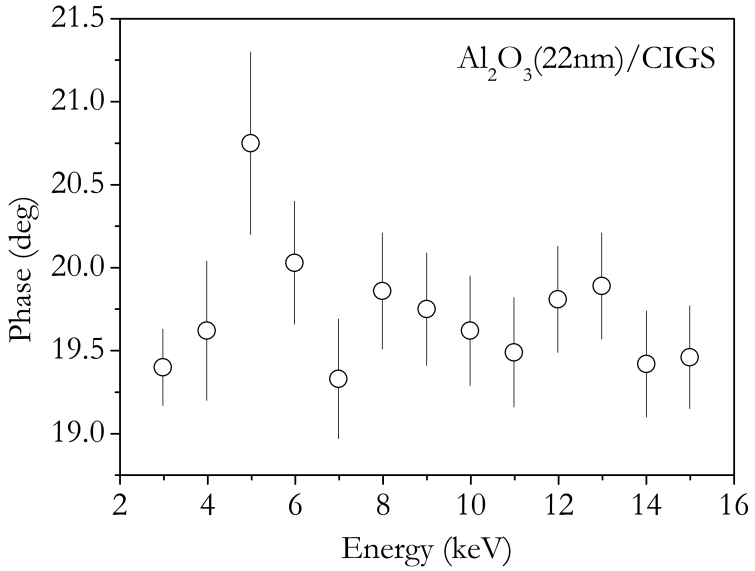

Fig. 3.3.1. Initial phase as a function of muon implantation energy, in a Al_2O_3(22nm) /CIGS sample, at 40 K.

The initial phase in Fig. 3.3.1 is constant, within the uncertainties, for different

implantation energies.

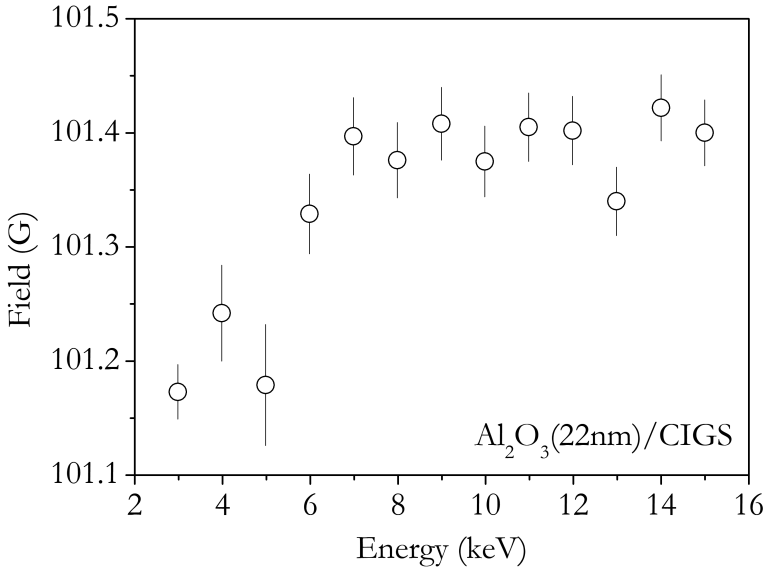

Fig. 3.3.2. Magnetic field at muon site as a function of muon implantation energy, in a Al_2O_3(22nm)/CIGS sample, at 40 K.

The magnetic field at muon site (Fig. 3.3.2) at low implantation energies corresponds to the externally applied magnetic field, and then increases for the CIGS region.

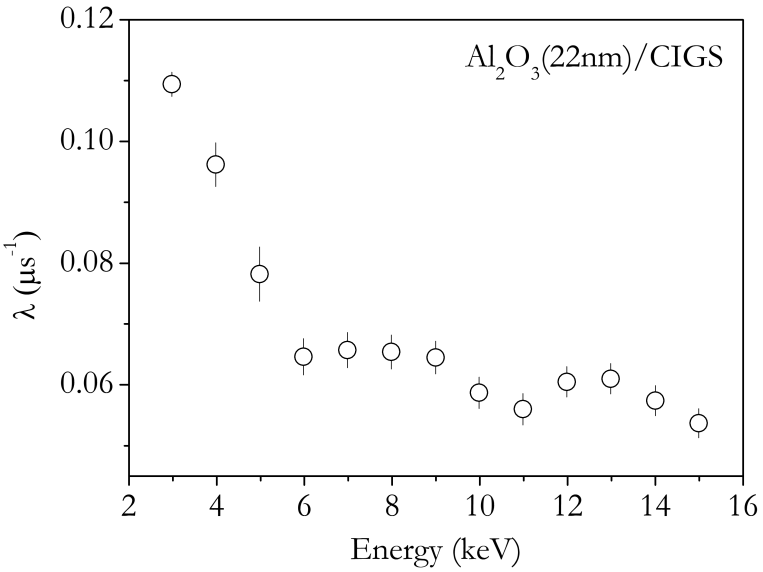

Fig. 3.3.3. Muon spin relaxation, λ, as a function of muon implantation energy, in a Al_2O_3(22nm)/CIGS sample, at 40 K.

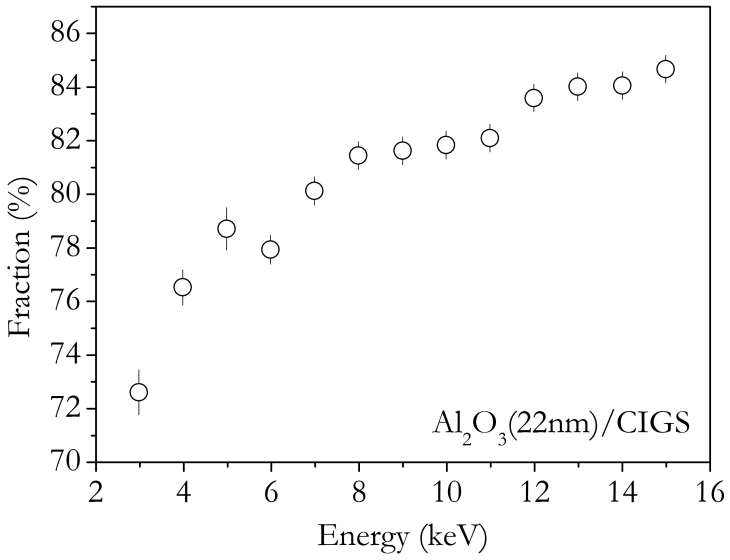

Fig. 3.3.4. Diamagnetic fraction as a function of muon implantation energy, in a Al_2O_3(22nm)/CIGS sample, at 40 K.

3.3.2 Depth-resolved analysis

After the conclusions taken from the article showcased in section 2.2.2 [AVV+18], and during the analysis of these results, it was decided that it would be useful to develop a method of obtaining depth-resolved information from the implantation energy dependence of the experimental parameters in a LEM experiment. Such method would be useful not only for the current work, but also for future projects in the scientific community that involve any type of sample in a LEM experiment. The content of this section will be the subject of an article to be submitted to the journal "Review of Scientific Instruments".

Upon implantation in a thin film or heterostructure, the muon stopping distribution depends on the muon implantation energy and density of the implanted materials. This implantation can be simulated using Monte Carlo simulations, more specifically with the Trim.SP code [Eck91], allowing to calculate the muon stopping distributions for different implantation energies [MGP+02], as can be seen in Fig. 3.3.5.

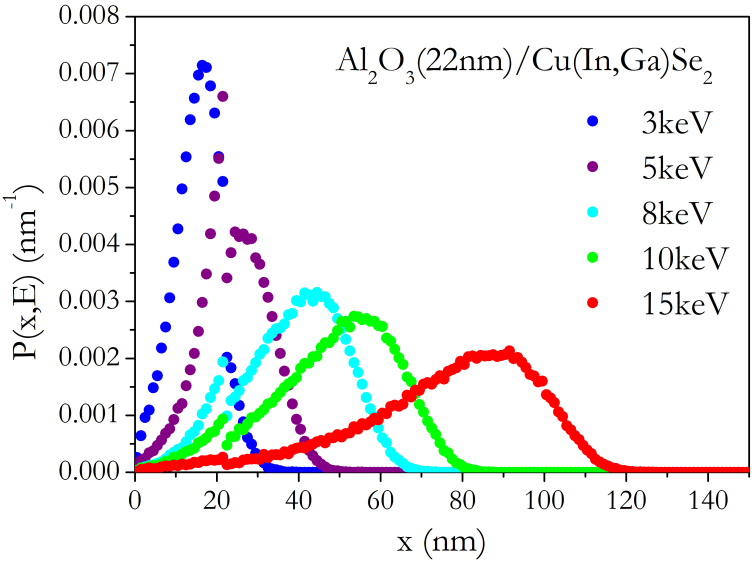

Fig. 3.3.5. Monte Carlo simulations of the probability per unit length, $P(x, E)$, that a muon implanted with energy E stops at a depth x in a Al_2O_3/CIGS junction, with a Al_2O_3 layer thickness of 22nm and an average CIGS composition of $Cu._{87}In._{61}Ga._{39}Se_2$. The different curves correspond to different muon implantation energies.

The Al_2O_3(22nm)/CIGS sample for which a basic analysis was already presented in the previous section, is used in this section as an example to explain the depth-resolved analysis method.

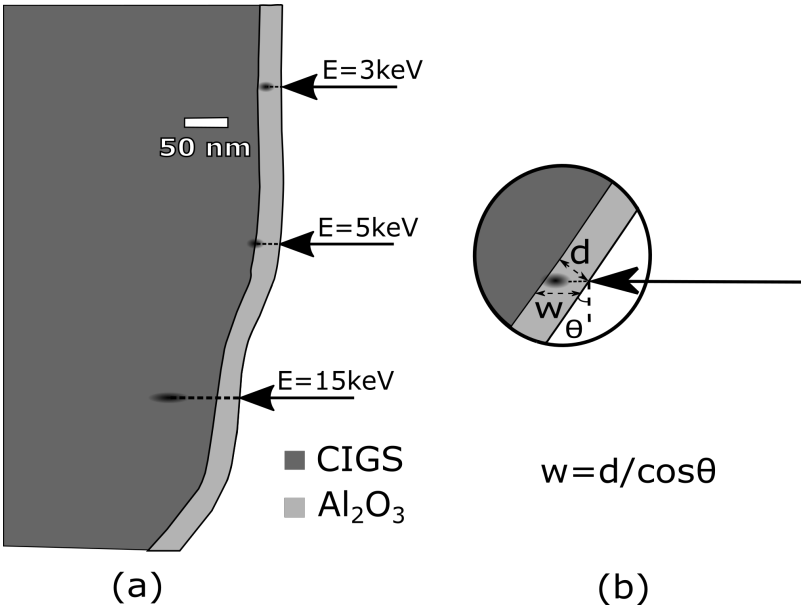

Fig. 3.3.6. a) Representation of the different implantation depths achieved with different muon implantation energies, for an Al_2O_3/CIGS heterostructure. The drawing is based on the respective TEM picture from Fig. 3.1.3. **b)** Detailed area to show the effect of the roughness of the film surface: the effective width of the surface layer seen by the muon probe, w, is larger than its nominal width, d, and depends on the average value of the inclination of the film surface relative to the direction of the muon beam.

While the width of Al_2O_3 measured by TEM in the INL yielded 22±4 nm, it is important to point out that the effective width of the Al_2O_3 layer seen by the muon probe is larger than its nominal width due to the roughness of the layer, with the effective width depending on the inclination of the film surface relative to the direction of the muon beam, as illustrated in Fig. 3.3.6 (b). Despite this, the TEM images suggest that this widening is not larger than 5 nm, meaning that the 22±4 nm can be taken as the reference value for the Al_2O_3 layer with of this sample.

As can be observed in Fig. 3.3.5, the muon stopping range extends in a relatively broad region inside the sample, meaning that the depth resolution of the μSR experiment is not sufficient to convert directly the energy dependence of a given μSR parameter (refereed here as $f(E)$) into a depth dependence, $f(x)$, making it difficult

to identify and study phenomena in multi-layered structures.

The method we propose aims to infer the depth dependence of a certain μSR parameter consistent with the experimental data. The approach we propose is similar in principle to what was done in section 2.2.2, which is dividing the sample into layers, assuming that the μSR parameter is constant within each layer. In the case of this sample, it is reasonable to expect at least two layers: $0 < x < a$ and $x > a$, where a is the layer width. The f values for each layer would be the characteristic Al_2O_3 and CIGS values, respectively. In reality, the changes in the μSR parameters are expected to be a continuous function, but the assumption of abrupt changes of the parameters can be a good approximation in a two-layer system, considering both the composition change and the limited experimental depth resolution. It also makes it easier to interpret the magnitude and extent of the variations of the parameters. However, some parameters may exhibit a change of f within a given material, for example, close to the interface of two materials, requiring an additional near-interface region for $f(x)$.

For the case where the experimental data suggests that $f(x)$ involves three main regions, the simplest approach is to assume that $f(x)$ is a step-like function given by:

$$f(x) = \begin{cases} f_{0a} & \text{for} \quad 0 \leq x \leq a\,, \\ f_{ab} & \text{for} \quad a \leq x \leq b\,, \\ f_{b\infty} & \text{for} \quad x \geq b\,, \end{cases} \tag{3.6}$$

where f_{0a}, f_{ab} and $f_{b\infty}$ are the average values of the μsR parameter f in the respective depth ranges.

With this model, $f(E)$ is calculated as:

$$f(E) = p_{0a}(E)\, f_{0a} + p_{ab}(E)\, f_{ab} + p_{b\infty}(E)\, f_{b\infty} \tag{3.7}$$

where $p_{0a}(E)$, $p_{ab}(E)$ and $p_{b\infty}(E)$ are the probabilities that a muon with energy E stops in the respective depth range. The values of f_{0a}, f_{ab}, $f_{b\infty}$, a and b are adjustable parameters used to obtain the function $f(E)$ that describes the experimental data.

As mentioned before, it is possible to obtain the muon stopping probability per unit length, $P(x, E)$, for different implantation energies, in a given material, by Monte Carlo simulation, using the code TRIM.SP. This is exemplified in Fig. 3.3.7 for an

implantation energy of 15 keV, considering the Al_2O_3(22nm)/CIGS sample.

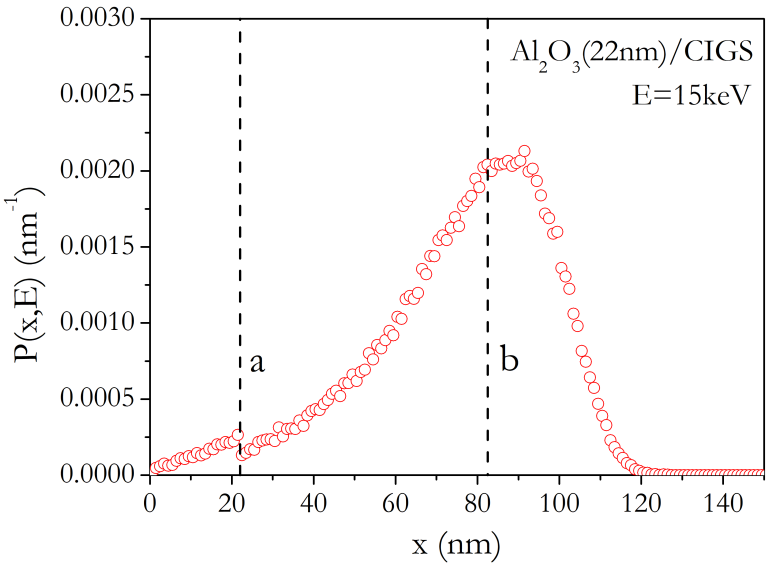

Fig. 3.3.7. Results from Monte Carlo calculations for the muon stopping probability per unit length, $P(x, E)$, in a Al_2O_3(22nm)/CIGS sample, as a function of implantation depth, x, for a muon implantation energy E = 15 keV. This calculation was executed for all the experimental muon implantation energies, and for some additional implantation energies as well. Integrating the curve in the ranges $0 < x < a$, $a < x < b$ and $b < x < \infty$ yields the corresponding probabilities $p_{0a}(E)$, $p_{ab}(E)$ and $p_{b\infty}(E)$, that the muons stop in each of the selected regions.

Upon obtaining the muon stopping probability per unit length $P(x, E)$ values, the probability $P_{ab}(E)$ that a muon implanted with energy E stops in the range $a < x < b$ can be calculated by numerical integration of $P(x, E)$ over the chosen range:

$$P_{ab}(E) = \int_a^b P(x, E)dx \tag{3.8}$$

This model can be refined to encompass a smooth transition between two different values of f. For example, if the regions $a < x < b$ and $x > b$ are both in the CIGS side of the sample, the following alternatives to equations 3.6 and 3.7 can be considered:

$$f(x) = \begin{cases} f_{0a} & \text{for} \quad 0 \leq x < a\,, \\ f_{ab} & \text{for} \quad a \leq x < b\,, \\ f_{c\infty} + \frac{f_{ab} - f_{c\infty}}{1+\mathrm{e}^{x-x_0/d}} & \text{for} \quad b \leq x \leq c\,, \\ f_{c\infty} & \text{for} \quad x \geq c\,, \end{cases} \tag{3.9}$$

where $x_0 = \frac{b+c}{2}$ and $f(E)$ is given by:

$$f(E) = p_{0a}(E)\, f_{0a} + p_{ab}(E)\, f_{ab} + \int_b^c P(x,E) f(x) dx + p_{c\infty}(E)\, f_{c\infty} \tag{3.10}$$

In this case there is a sigmoidal transition between the f_{ab} and $f_{c\infty}$, that is, in the range $b \leq x \leq c$. There are two additional parameters in this case, the parameters c and d, that determine the width of the transition region and the slope of the transition between f_{ab} and $f_{c\infty}$, respectively.

Considering the three-step case, when making the analysis, initial values for the parameters a, b, f_{0a}, f_{ab} and $f_{b\infty}$ are inferred by visual inspection of the experimental data. The function $f(E)$, which is the function fitted to the experimental data, is calculated with equation 3.7, using a, b, f_{0a}, f_{ab} and $f_{b\infty}$ as the free parameters. As mentioned before, if a smooth transition is considered, there are two additional parameters c and d that determine the width and the smoothness of the transition respectively. In that case, d must be constrained to vary within a range that ensures that $f(E)$ becomes constant when it approaches the edges of the transition layer (smooth region).

A MATLAB routine was developed to fit the experimental μSR parameters as a function of muon implantation energy, using the model presented here. The routine calculates a theoretical $f(E)$ function as described, and then utilizes the Fminuit [All16] program to fit the function to the experimental $f(E)$ data. Fminuit is a free optimization and chi-square fitting program for MATLAB, based on the Minuit minimization package developed at CERN. The final parameters obtained from the fit are used to generate the depth dependent function $f(x)$ that corresponds to the best description of the experimental data. This MATLAB routine was developed with the intention of making it available for the μSR community. The corresponding

instruction manual is presented in Appendix A.

From the experimental data in section 3.3.1 it is observed that all the μSR parameters exhibit changes with the muon implantation, except the initial phase. Therefore, the parameter ϕ will be ignored in the following discussion.

Fig. 3.3.8 (Left) shows the muon spin relaxation λ and the local magnetic field, as a function of muon implantation energy. The data was analysed assuming two layers with an abrupt change of the parameters at the interface, as seen in Fig. 3.3.8 (Right). The parameters obtained from the fit are presented in Table 3.3.1.

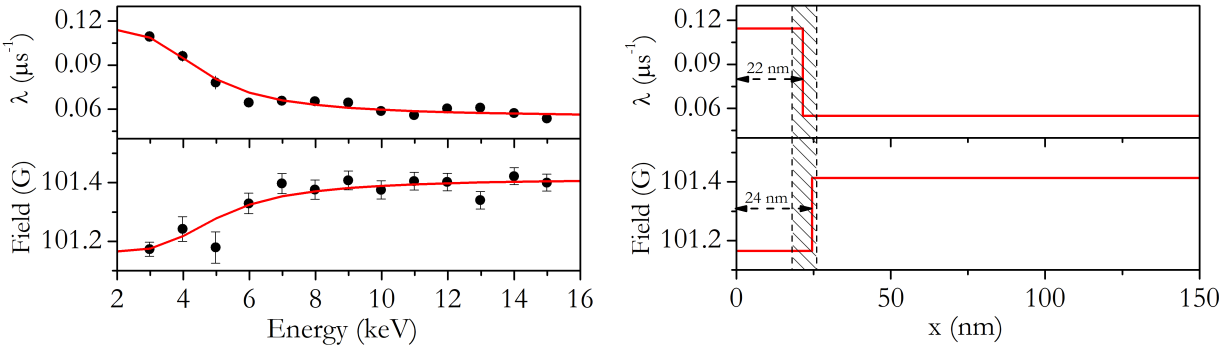

Fig. 3.3.8. Left: Experimental muon spin relaxation, λ, and local magnetic field at the muon position as a function of muon implantation energy, at 40 K. The red curve is the predicted behaviour of the parameters assuming a depth dependence, as shown in the corresponding graph at right. **Right:** The functions $\lambda(x)$ and Field(x) are assumed to have a step-like function with two regions. The dashed areas represent the position obtained from TEM for the interface between the Al_2O_3 and CIGS layers.

	λ (μs^{-1})	Effective Field (G)
Al_2O_3	0.114(2)	101.17(3)
CIGS	0.055(1)	101.41(1)
1st layer width (nm)	22(1)	24(3)
χ^2_{red}	1.4	1.1

Table 3.3.1. Fitting parameters and reduced chi-square value obtained in the fitting analysis of the relaxation rate (λ) and effective magnetic field.

The full curves obtained in the fits are a good description of the data, proving the potential of assuming a step-like function. There was also an attempt to perform the

fit using a smooth transition, yet the description proved to be significantly worst than the one obtained simply with two steps, with the fitting parameter d always converging to the limit of an abrupt transition. Note that the width of the first layer obtained with the fit is consistent with the width of the Al_2O_3 obtained in the TEM analysis. This shows that for both the muon relaxation rate and the local field at the muon site, the changes with depth are only due to composition changes. While the relaxation value in the CIGS material may seem lower than previously observed, this is only due to the choice of the Lorentzian shape for the relaxation function, with the behaviour in fact being consistent with previous observations [AVG+14][AVV+18][PME+07]. Concerning the effective magnetic field at the muon site, it is just the externally applied field for the Al_2O_3 region, whereas it is slightly higher in the CIGS region, suggesting that the apparent diamagnetic signal contains a paramagnetic component, which is also consistent with previous reports [AVV+18].

For the analysis of the diamagnetic fraction f_{dia}, three different approaches were attempted (Fig. 3.3.9), with the final fitting parameters being presented in Table 3.3.2.

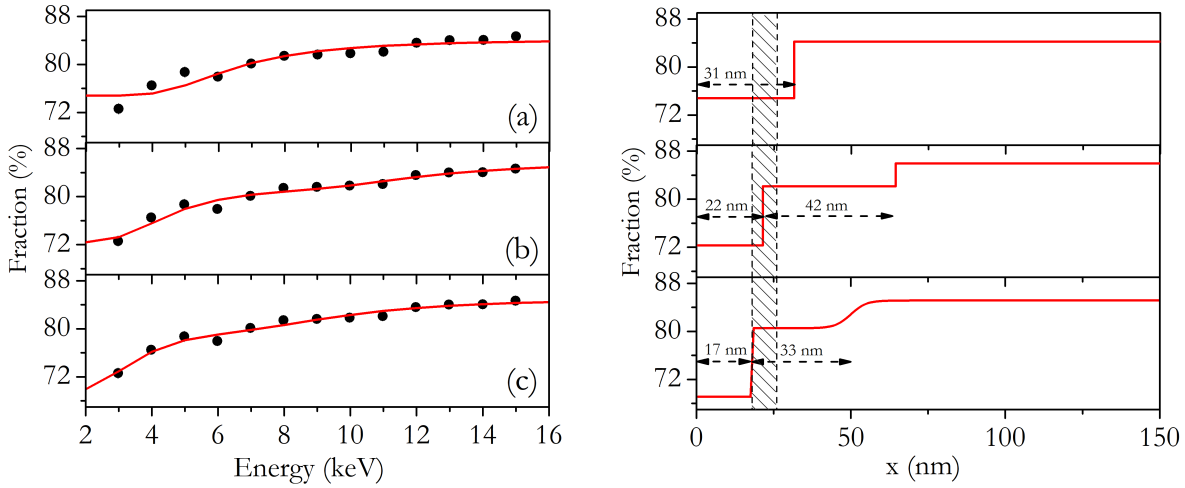

Fig. 3.3.9. Left: Experimental diamagnetic fraction as a function of muon implantation energy, $f_{dia}(E)$, at 40 K. The red curve is the predicted behaviour of the parameters assuming a depth dependence, as shown in the corresponding graph at right. **Right:** In (a) the function $f_{dia}(x)$ is assumed to be a two step function, in (b) is is assumed to be a three step function and in (c) it is assumed to have a smooth change inside CIGS. The dashed areas represent the position obtained from TEM for the interface between the Al_2O_3 and CIGS layers.

	Diamagnetic Fraction (%)		
	(a)	(b)	(c)
Al_2O_3	74.8(9)	72.3(8)	69.2(86)
CIGS (close to the interface)	84.2(3)	82.1(3)	80.5(9)
CIGS (bulk)	84.2(3)	86.0(5)	85.1(4)
1^{st} layer width (nm)	31(4)	22(1)	17(2)
2^{st} layer width (nm)	-	42(3)	33(10)
χ^2_{red}	3.0	1.6	1.7

Table 3.3.2. Fitting parameters and reduced chi-square value obtained in the depth-resolved analysis of the diamagnetic fraction, for three distinct fit approaches, (a), (b) and (c), depicted in Fig 3.3.9.

Considering the previous approach of having two regions with an abrupt change of the parameter at the interface (Fig. 3.3.9 (a)), the description of the data is poor, with an associated χ^2_{red}=3.0. This suggests that an additional region should be considered for the $f_{dia}(x)$ function. It is important to note that the experimental data $f_{dia}(E)$ does not, by itself, give any clue about where the third region is located (within Al_2O_3, CIGS, or both) neither about its spatial extent. This additional region can be observed in Fig. 3.3.9 (b), with abrupt changes between the three regions, and in Fig. 3.3.9 (c), where a smooth transition was allowed between the second and third region. The improvement in the fit clearly justifies adding a third region, as can be seen by reduced chi-square values, and even just by visual inspection of the fits. In both (b) and (c), the final f_{dia} function clearly shows that the intermediate region is on the CIGS side, close to the Al_2O_3 interface. Since it is unlikely that that a transition within CIGS is abrupt, option (c) is probably closer to reality. However, the fit results in Table 3.3.2 suggests that this refinement does not lead to a improvement in the description of the data.

Therefore, description (b) was chosen as the best one between the three to draw conclusions from, as it is the one with the best compromise between fit quality and complexity. It can be observed in with greater detail in Fig. 3.3.10.

Evidences about the existence of two regions with the CIGS material with different formation probabilities of the diamagnetic muon state were already reported

in CdS/CIGS and ZnSnO/CIGS heterostructures [AVV+18], and were interpreted as due to a disordered region in CIGS, close to the interface with the adjacent material. In this Al_2O_3/CIGS system the effect is much less evident in the experimental data, when compared with the data from CdS/CIGS and ZnSnO/CIGS, but its presence is revealed by the depth-resolved analysis.

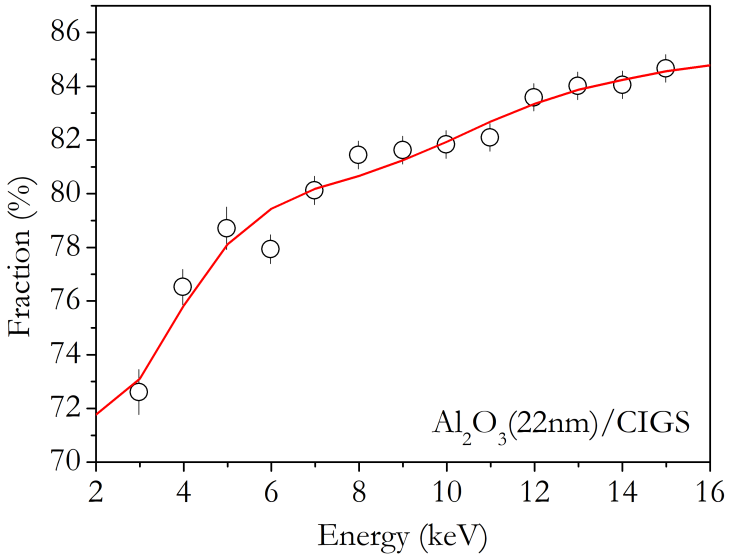

Fig. 3.3.10. Experimental diamagnetic fraction as a function of muon implantation energy, in a Al_2O_3(22nm)/CIGS sample, at 40 K. The red curve is the predicted behaviour using a depth-resolved analysis. The parameters are presented in Table 3.3.2 (b)

3.4 Al_2O_3(4nm)/CIGS

After doing the WiMDA analysis for the Al_2O_3(4nm)/CIGS as a function of muon implantation energy, the following results were obtained for the different μSR parameters:

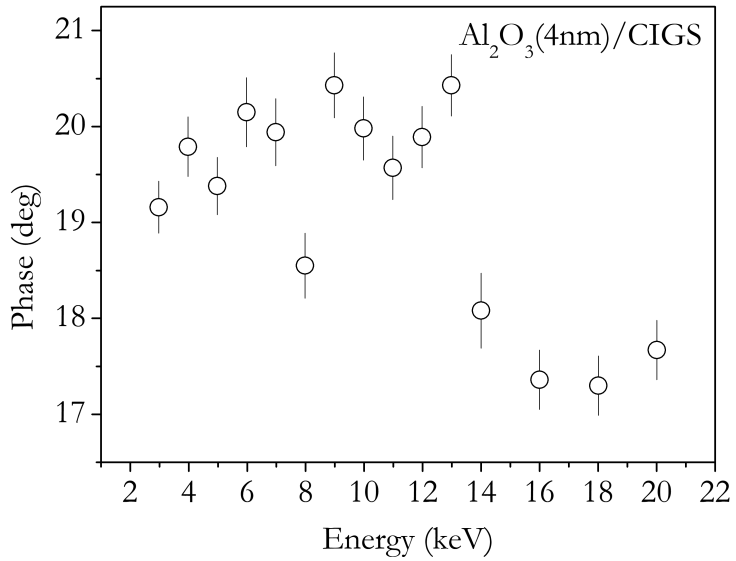

Fig. 3.4.1. Initial phase as a function of muon implantation energy, in a Al_2O_3(4nm) /CIGS sample, at 40 K.

The phase shift at above 14 keV is an experimental artefact. It is due to the generation of secondary electrons at the sample surface that travel back to the trigger detector and generate a wrong start signal. This effect is also present in a silver sample used for calibration, as well as in data from the CdS/CIGS and CdS/Al_2O_3/CIGS samples.

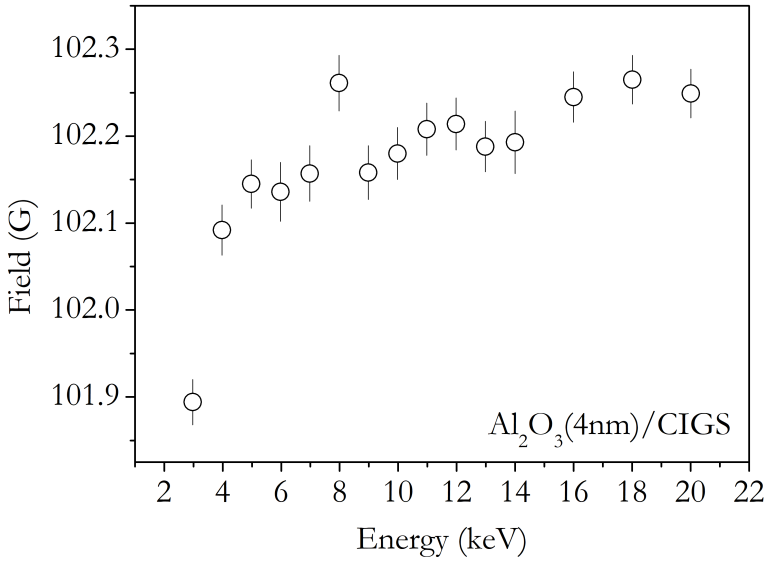

Fig. 3.4.2. Magnetic field at muon site as a function of muon implantation energy, in a Al_2O_3(4nm)/CIGS sample, at 40 K.

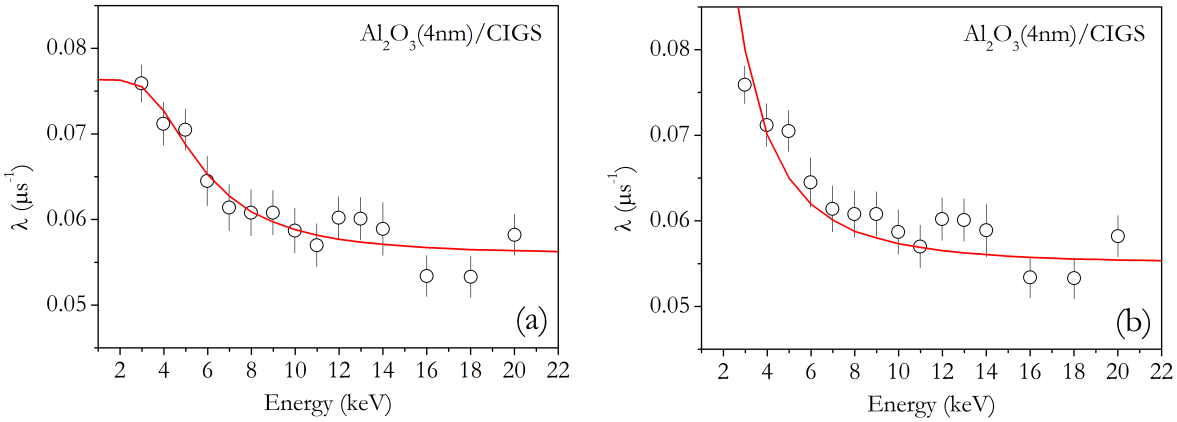

Fig. 3.4.3. Muon spin relaxation, λ, as a function of muon implantation energy, in a Al_2O_3(4nm)/CIGS sample, at 40 K. The red curves are the predicted behaviour using a depth-resolved analysis, being that in **(a)** the fit is performed with the parameters kept free, and in **(b)** the fit is performed constraining the λ values to those of the Al_2O_3(22nm)/CIGS sample, from Table 3.3.1. The parameters for this case are in Table 3.4.1.

	f_1 (μs^{-1})	f_2 (μs^{-1})	Layer width (nm)
(a)	0.076(3)	0.056(1)	33(5)
(b)	0.114(0)	0.055(0)	16(1)

Table 3.4.1. Fitting parameters obtained in the depth-resolved analysis of the muon spin relaxation, λ, for the case of the Al_2O_3(4nm)/CIGS sample, at 40 K. **(a)** The fit is performed with the parameters kept free. **(b)** The fit is performed constraining the λ values to those of the Al_2O_3(22nm)/CIGS sample, from Table 3.3.1.

The muon spin relaxation can be observed in Fig. 3.4.3. Two fitting approaches, in images (a) and (b), were used to draw conclusions from this data, considering in both that the behaviour can be modelled by two regions, correspondent to Al_2O_3 and to CIGS.

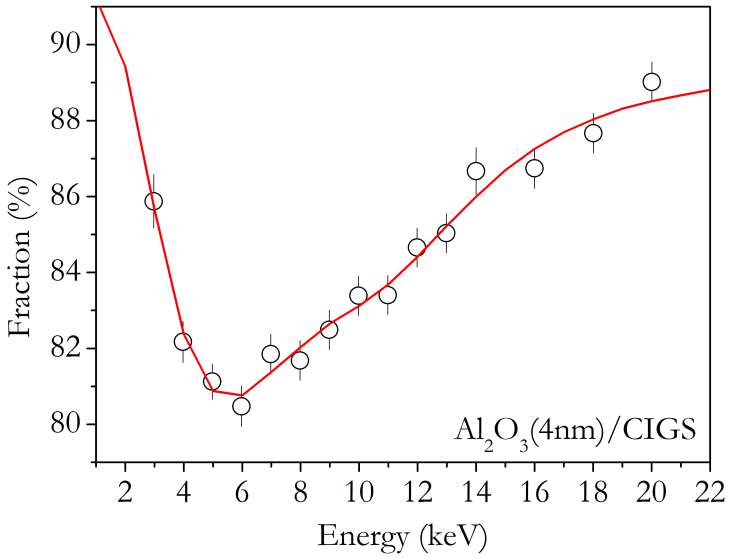

Fig. 3.4.4. Experimental diamagnetic fraction as a function of muon implantation energy, , in a Al_2O_3(4nm)/CIGS sample, at 40 K. The red curve is the predicted behaviour using a depth-resolved analysis. The parameters are presented in Table 3.3.2 (b)

	f_1 (%)	f_2 (%)	f_3 (%)	f_4 (%)
Al_2O_3(4nm)/CIGS	91.5(63)	76.0(15)	84.4(3)	89.5(4)

1st layer (nm)	2nd layer (nm)	3rd layer (nm)
22(1)	22(2)	42(2)

Table 3.4.2. Fitting parameters obtained in the depth-resolved analysis of the diamagnetic fraction, for the case of the Al_2O_3(4nm)/CIGS sample.

The depth-resolved analysis of the experimental muon spin relaxation (Fig. 3.4.3 and Table 3.4.1) shows that the first λ value is very different from the one observed in the Al_2O_3(22nm)/CIGS, which is unexpected. The behaviour of this parameter should be common in the two samples, with the only difference being the depth value at which the λ of Al_2O_3 changes to the λ of CIGS, but this does not happen. With free parameters the width of the Al_2O_3 layer is 33 nm, and by forcing the previous values from Al_2O_3(22nm)/CIGS the width is 16 nm. None of these values is consistent with the 4 nm of Al_2O_3 measured by TEM for this sample.

The diamagnetic fraction for this case is also hard to understand. The rapid decrease of the diamagnetic fraction near the surface means that a good description of the data can only be obtained with four steps (Fig. 3.4.4). The high initial $f(x)$ value of 91.5% suggests that the layer material differs from pure Al_2O_3, possibly due to an amorphous structure or even chemical mixing with CIGS. This is not too surprising since the Al_2O_3 film deposited on top of CIGS is very thin. Also its presence appears to affect CIGS until very deep in the sample, even more than for the case of Al_2O_3(22nm).

There results raise questions about the average composition of the sample at the surface, which requires further investigation in future work.

3.5 CdS(59nm)/CIGS

After doing the WiMDA analysis for the CdS(59nm)/CIGS as a function of muon implantation energy, the following results were obtained for the different μSR parameters:

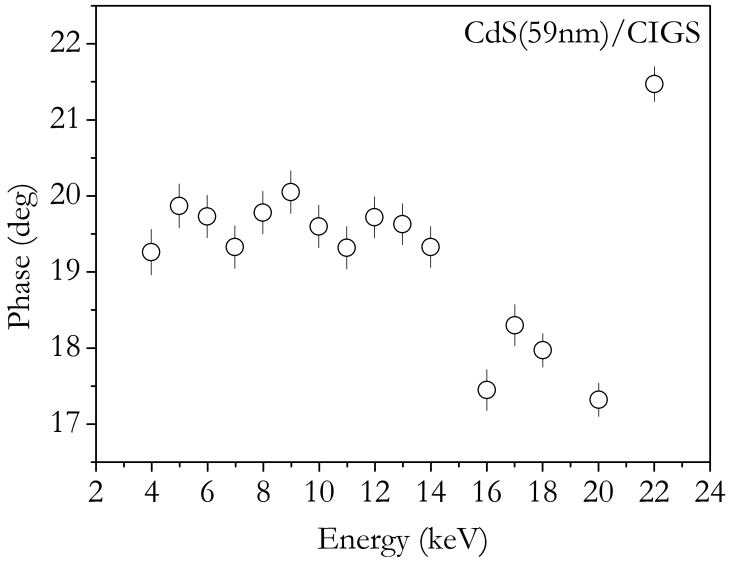

Fig. 3.5.1. Initial phase as a function of muon implantation energy, in a CdS(59nm) /CIGS sample, at 40 K.

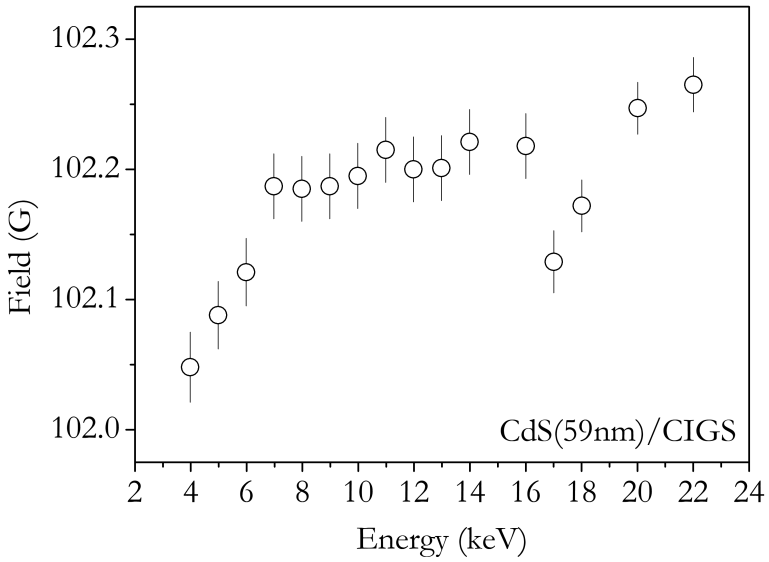

Fig. 3.5.2. Magnetic field at muon site as a function of muon implantation energy, in a CdS(59nm)/CIGS sample, at 40 K.

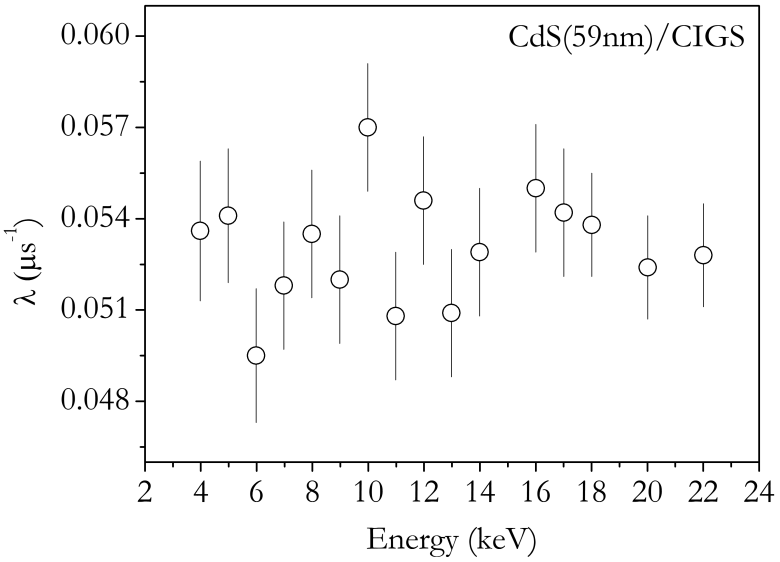

Fig. 3.5.3. Muon spin relaxation, λ, as a function of muon implantation energy, in a CdS(59nm)/CIGS sample, at 40 K.

In the cases of the CdS(59nm)/CIGS and CdS(47nm)/Al_2O_3(4nm)/CIGS samples there were runs performed with an implantation energy of 22 keV, for which the moderator voltage is set to 18 kV, which causes a very negative tension at the sample holder ($\sim$ -5 kV). This leads to secondary electrons being emitted towards the detector that starts the clock. The clock is then stopped randomly by decaying muons, resulting in a decrease in asymmetry. This phenomenon causes an additional shift in the initial phase.

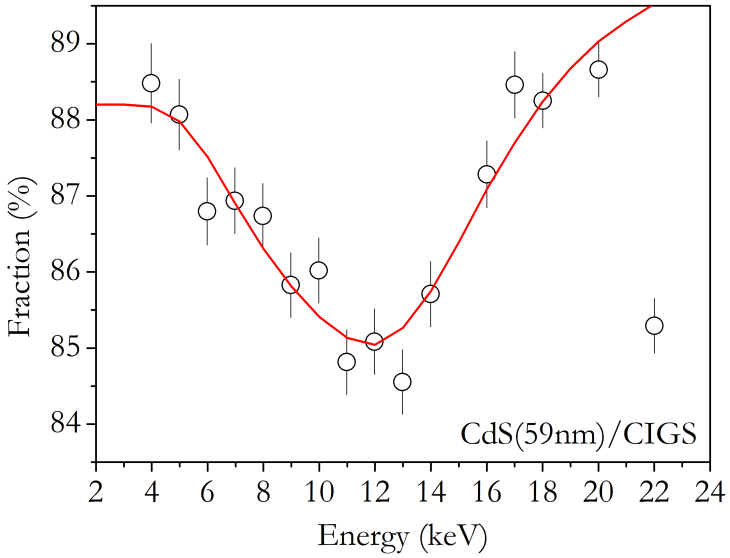

Fig. 3.5.4. Experimental diamagnetic fraction as a function of muon implantation energy, in a CdS(59nm)/CIGS sample, at 40 K. The red curve is the predicted behaviour using a depth-resolved analysis. The parameters are presented in Table 3.3.2 (b)

	f_1 (%)	f_2 (%)	f_3 (%)	1st layer (nm)	2nd layer (nm)
CdS/CIGS	88.2(3)	84.0(4)	90.5(5)	58(3)	45(5)

Table 3.5.1. Fitting parameters obtained in the depth-resolved analysis of the diamagnetic fraction, for the case of the CdS(59nm)/CIGS sample.

3.6 CdS(47nm)/Al_2O_3(4nm)/CIGS

After doing the WiMDA analysis for the CdS(47nm)/Al_2O_3(4nm)/CIGS as a function of muon implantation energy, the following results were obtained for the different μSR parameters:

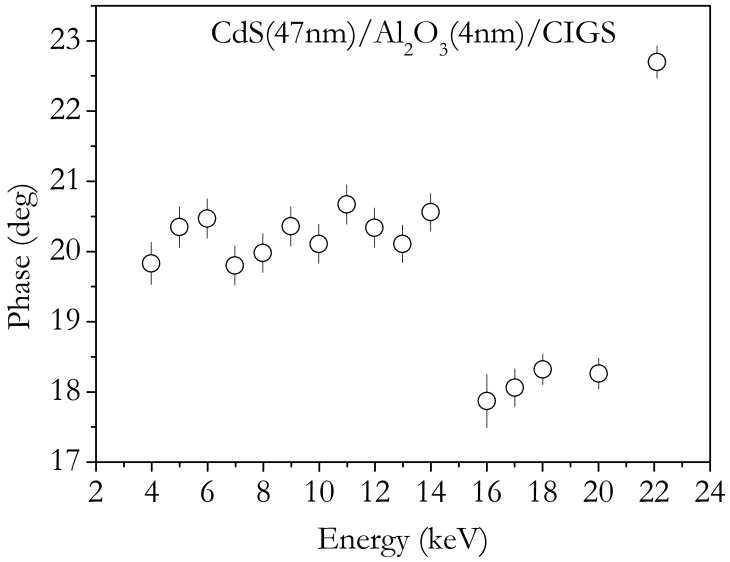

Fig. 3.6.1. Initial phase as a function of muon implantation energy, in a CdS(47nm) /Al_2O_3(4nm)/CIGS sample, at 40 K.

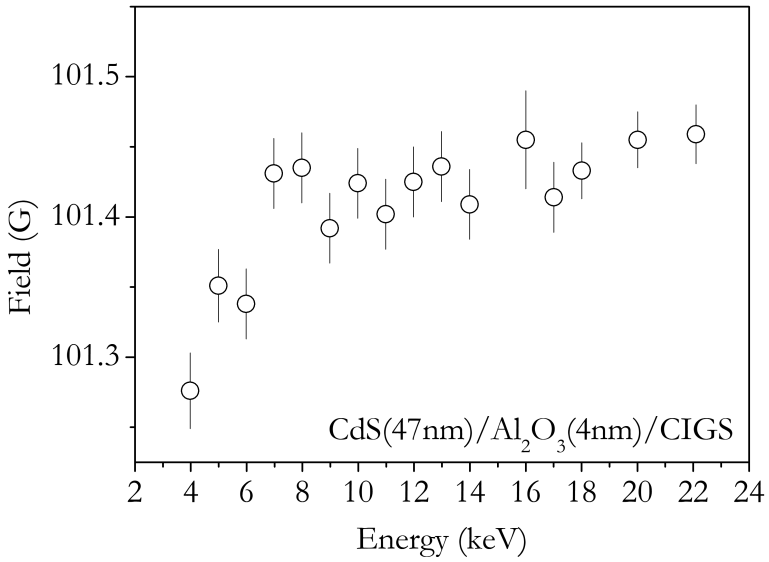

Fig. 3.6.2. Magnetic field at muon site as a function of muon implantation energy, in a CdS(47nm)/Al_2O_3(4nm)/CIGS sample, at 40 K.

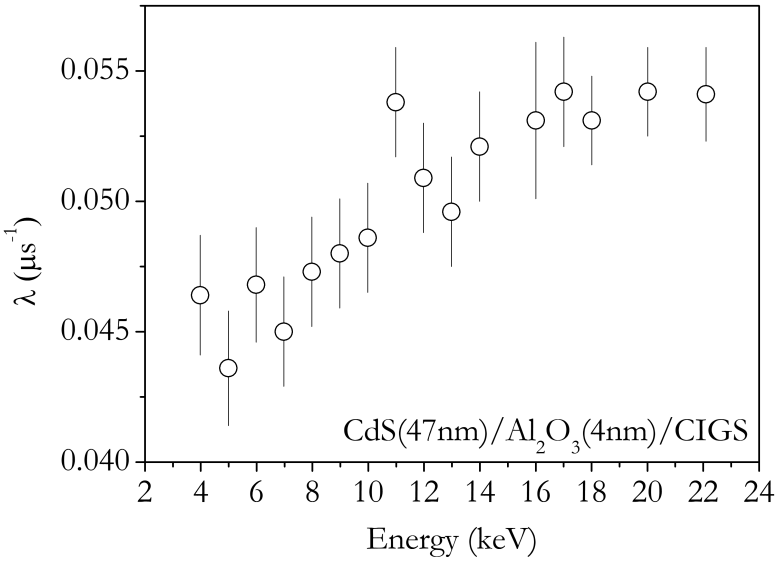

Fig. 3.6.3. Muon spin relaxation, λ, as a function of muon implantation energy, in a CdS(47nm)/Al_2O_3(4nm)/CIGS sample, at 40 K.

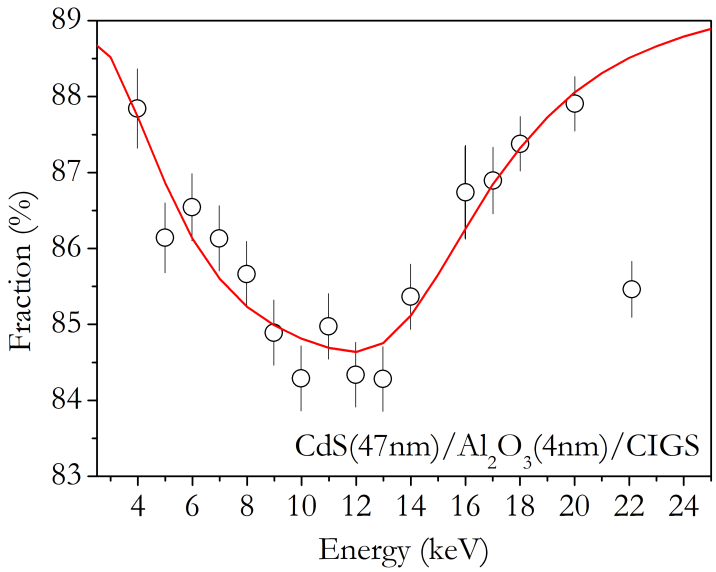

Fig. 3.6.4. Experimental diamagnetic fraction as a function of muon implantation energy, in a CdS(47nm)/Al_2O_3(4nm)/CIGS sample, at 40 K. The red curve is the predicted behaviour using a depth-resolved analysis. The parameters are presented in Table 3.3.2 (b)

	f_1 (%)	f_2 (%)	f_3 (%)	1st layer (nm)	2nd layer (nm)
CdS/Al_2O_3/CIGS	88.9(6)	84.2(2)	89.4(5)	41(3)	63(3)

Table 3.6.1. Fitting parameters obtained in the depth-resolved analysis of the diamagnetic fraction, for the case of the CdS(47nm)/Al_2O_3(4nm)/CIGS sample.

3.7 CIGS

The CIGS data presented in section 2.2.2, from [AVV+18], was re-analysed, this time with the new method.

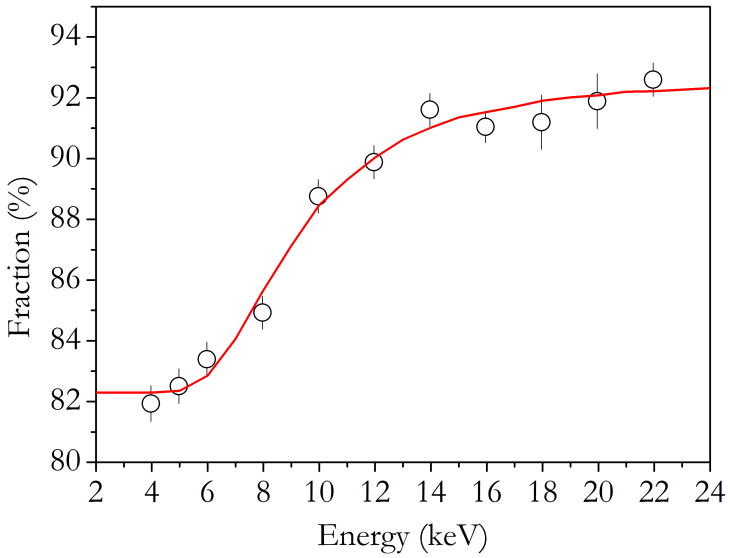

Fig. 3.7.1. Experimental diamagnetic fraction as a function of muon implantation energy, at 50 K. The red curve is the predicted behaviour using a depth-resolved analysis. The parameters are presented in Table 3.3.2 (b)

	f_1 (%)	f_2 (%)	Layer width (nm)
CIGS (bulk)	82.3(4)	92.6(3)	55(2)

Table 3.7.1. Fitting parameters obtained in the depth-resolved analysis of the diamagnetic fraction, for the case of the CIGS sample.

Chapter 4

Conclusions and future perspectives

4.1 Depth-resolved analysis tool

The main focus of this thesis ended up being the development of a method to extract depth-resolved information from the muon probe in a LEM experiment. In these experiments the experimental parameters are obtained as a function of the muon implantation energy, but if the energy dependent data exhibits an effect, inferring the corresponding depth dependent function may be crucial to understand the contribution of each layer for the effect, their spatial position and depth extent.

The method requires assuming a function for the depth dependence with variable parameters that are adjusted in order to describe the experimental energy dependent data. A simple approach of dividing the sample in layers and assuming step functions for the depth dependence has proven to be a good approximation. Attempts to refine this model proved to be mostly unsuccessful at improving the quality of the fit, possibly due to the limited depth resolution of the muon probe.

In this thesis the use of this method was exemplified for four semiconductor heterostructures, but it can be applied to any material used in a LEM experiment. Therefore it constitutes a general tool for the analysis of slow muon experiments.

4.2 CIGS results

In Fig. 4.2.1 the experimental diamagnetic fractions for the samples, already presented in the last section, are displayed together to facilitate their visual analysis. The Al_2O_3(4nm)/CIGS sample was left out of it, since the results raised questions that require further investigation.

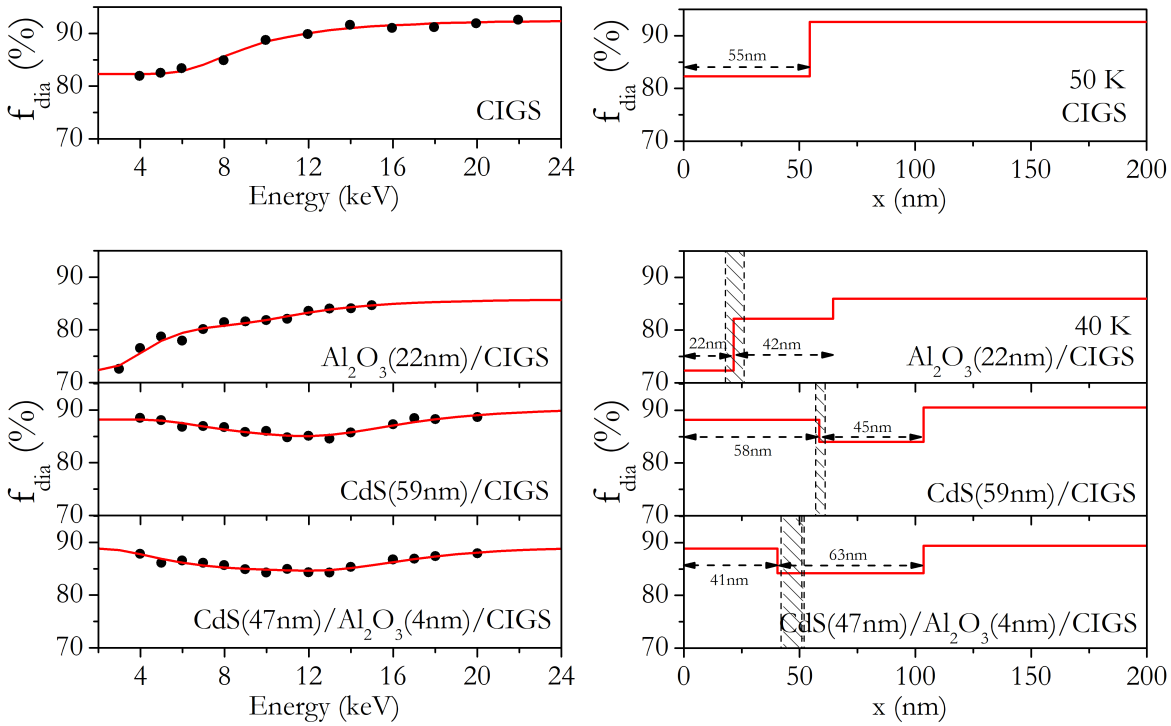

Fig. 4.2.1. Experimental diamagnetic fraction as a function of muon implantation energy, at 50 K (for CIGS) and 40 K (for the remaining samples). The red curve is the predicted behaviour using a depth-resolved analysis, with all parameters free. The corresponding parameters were presented in the sections for each sample in chapter 3.

The best fits are obtained when all the parameters are kept free, as shown in Fig. 4.2.1. The corresponding fitting parameters were already presented in the previous section. However, some constraints were imposed so that the results are acceptable from a physics point of view. Since all heterostructures were produced from a single CIGS sample, the diamagnetic fraction for CIGS in the bulk region should be common to all the heterostructures, and that constraint was forced in a new analysis for the

same samples, as seen in Fig. 4.2.2.

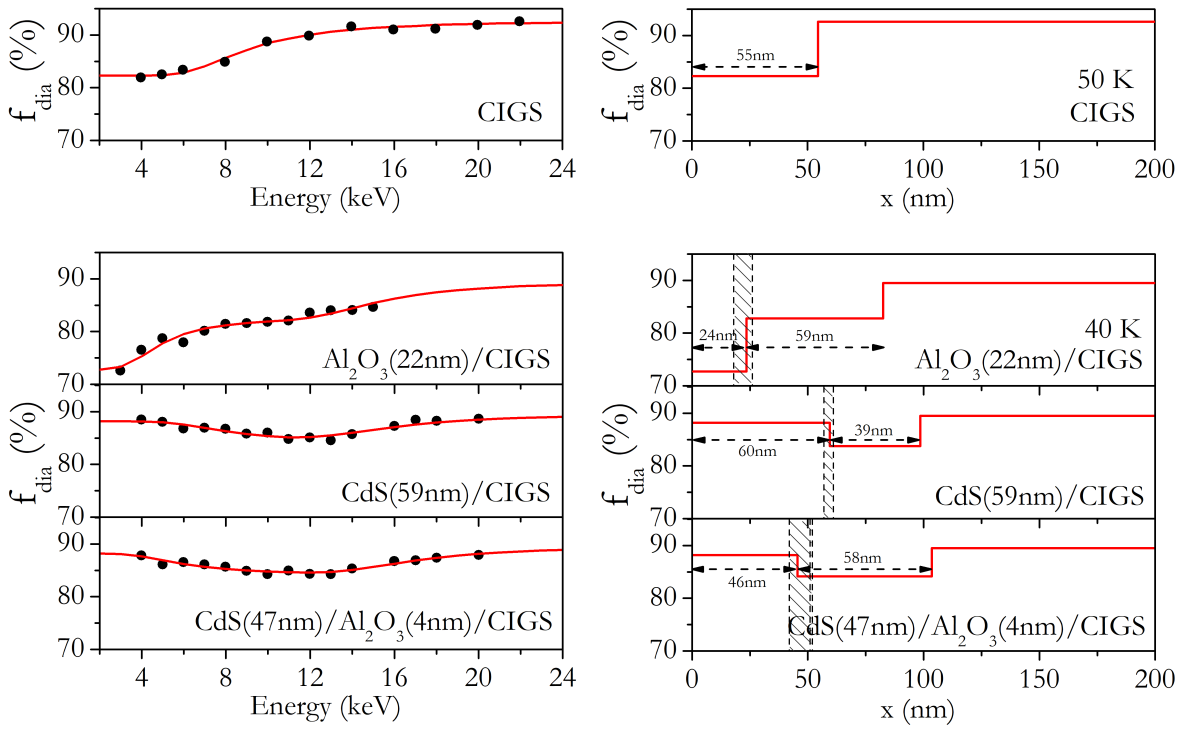

Fig. 4.2.2. Experimental diamagnetic fraction as a function of muon implantation energy, at 50 K (for CIGS) and 40 K (for the remaining samples). The red curve is the predicted behaviour using a depth-resolved analysis, where the diamagnetic value for CIGS was forced to be common to all the samples. The corresponding parameters are presented in Table 4.2.1.

	f_1 (%)	f_2 (%)	f_3 (%)	1st layer (nm)	2nd layer (nm)
CIGS (bulk)	82.3(4)	92.6(3)		55(2)	
Al_2O_3/CIGS	72.7(60)	82.8(10)	89.5(0)	24(1)	59(3)
CdS/CIGS	88.2(21)	83.7(19)	89.5(0)	60(4)	39(4)
CdS/Al_2O_3/CIGS	88.2(0)	84.1(4)	89.5(0)	46(4)	58(5)

Table 4.2.1. Fitting parameters obtained in the fitting analysis of the diamagnetic fraction in Fig. 4.2.2, for the different samples.

Other fitting approaches can be considered, such as fixing the widths of the surface layers to the value measured by TEM, and these will be tested in a future analysis. However, some general conclusions can be extracted from the data presented in Fig.

4.2.2 and in Table 4.2.1.

The value of CIGS $f_{CIGS} = 89.5\%$ was chosen as the best value for the Al_2O_3/CIGS, CdS/CIGS and CdS/Al_2O_3/CIGS graphs in Fig. 4.2.2. For the Al_2O_3(22nm)/CIGS sample, the data suggests that $f_{Al_2O_3} = 73(6)\%$, which is consistent with past results from bulk sapphire at low energies (5 keV) ([PME$^+$07]). In the CdS/CIGS and CdS/Al_2O_3/CIGS samples the diamagnetic fraction at the surface is $f_{CdS} = 88(2)\%$. This is less than expected for bulk CdS at this temperature. However, the μSR signal in the CdS layer deviates from bulk behaviour in other μSR parameters ([GAV$^+$99][GVPA01][ACC$^+$09]) such as relaxation, suggesting the film has a large concentration of impurities.

Regarding the case of the Al_2O_3(22nm)/CIGS sample, three steps in f_{dia} were necessary to describe the data. The width of the first step (a=24(1) nm) is consistent with the width of the Al_2O_3 layer obtained by TEM. The CIGS layer contains two regions. The region closer to the surface has a width of 59(3) nm. The CIGS alone (upper graph of Fig. 4.2.2) has a surface defect region with an extent of 55(2) nm. Therefore, within the uncertainties of the fitted parameters, no healing effect from the Al_2O_3 layer in CIGS is observed by the muon probe.

The data from the CdS(59nm)/CIGS sample is also better described by three steps. The first step is 60(4) nm wide, corresponding to the width of the CdS layer measured by TEM. The defected region in CIGS has a width of 39(4) nm, narrower than observed in the Al_2O_3/CIGS sample and in the CIGS film. This suggests that CdS produces a healing effect in the CIGS defect region, whereas Al_2O_3 does not.

In the case of the CdS(47nm)/Al_2O_3(4nm)/CIGS, the function $f_{dia}(x)$ is also described by three steps, with the first one having a width of 46(4) nm which matches, within uncertainties, the extent of the CdS layer. The width of the CIGS defect region is 58(5) nm, which is similar to the one observed in the CIGS film, and larger than the observed in CdS(59nm)/CIGS. This observation suggests that the Al_2O_3 layer blocks the healing effect of CdS in the CIGS defect region.

4.3 Future perspectives

The tool developed in this work proved useful for drawing conclusions from the gathered data, even though a more throughout interpretation of the results is due in the future.

Other materials for the surface passivation of CIGS and other passivation strategies will be studied in the future. There is already a proposal to study CIGS films with their surface passivated with silicon dioxide (SiO_2), using the LEM instrument at the PSI, and a proposal to use the ISIS Muon and Neutron Source, in the United Kingom, to study polycrystalline CIGS samples. In these future works the depth-resolved analysis tool is likely to be an important support tool for the data analysis.

Bibliography

[ABD+05] L. Assmann, J. C. Bernède, A. Drici, C. Amory, E. Halgand, and M. Morsli. Study of the Mo thin films and Mo/CIGS interface properties. *Applied Surface Science*, 246(1-3):159–166, 2005.

[ACC+09] H V Alberto, N Ayres De Campos, S F J Cox, J M Gil, J Piroto Duarte, and R C Vila. Spin exchange of muonium in CdS. *Physica B: Condensed Matter*, 404(5-7):834 – 836, 2009.

[Alb17] Marco Alberto. *High dielectric constant oxides for CMOS technology*. Master's thesis, Universidade de Coimbra, 2017. `https://estudogeral.sib.uc.pt/handle/10316/82960`.

[All16] Giuseppe Allodi. FMINUIT - A binding to Minuit for Matlab, Octave & Scilab, (accessed on 2019-06-16). `http://www.fis.unipr.it/{~}giuseppe.allodi/Fminuit/Fminuit{\_}intro.html`.

[Ama18] Alex Amato. Physics with Muons : From Atomic Physics to Solid State Physics - Lecture notes, 2018. `https://www.psi.ch/en/lmu/lectures`.

[AVG+14] H. V. Alberto, R. C. Vilão, J. M. Gil, J. Piroto Duarte, R. B.L. Vieira, A. Weidinger, J. P. Leitão, A. F. Da Cunha, M. G. Sousa, J. P. Teixeira, P. A. Fernandes, P. M.P. Salomé, K. Timmo, M. Loorits, A. Amato, H. Luetkens, T. Prokscha, A. Suter, and Z. Salman. Muonium states in Cu2ZnSnS4 solar cell material. *Journal of Physics: Conference Series*, 551(1):1–6, 2014.

[AVV+18] H V Alberto, R C Vilão, R B L Vieira, J M Gil, A Weidinger, M G Sousa, J P Teixeira, A F Cunha, J P Leitão, P M P Salomé, P A Fernandes, T Törndahl, T Prokscha, A Suter, and Z Salman. Slow-muon study of quaternary solar-cell materials : Single layers and p - n junctions. *Physical Review Materials*, 2(2):1–11, 2018.

[Ber17] V. Bermudez. Economical and operational issues for CIGS in the future PV panorama. *Solar Energy*, 146(April):85–93, 2017.

[Blu99] S J Blundell. Spin-polarized muons in condensed matter physics. *Contemporary Physics*, 40(3):175–192, 1999.

[BM04] Pavel Bakule and Elvezio Morenzoni. Generation and applications of slow polarized muons. *Contemporary Physics*, 45(3):203–225, 2004.

[Bro11] Gregory Ferguson Brown. *The Effects of Non-Uniform Electronic Properties on Thin Film Photovoltaics*. PhD thesis, University of California, Berkeley, 2011. `https://escholarship.org/uc/item/30t6135k`.

[CAS+19] M A Curado, H V Alberto, A F A Simões, J M Gil, T Prokscha, A Suter, Z Salman, J M V Cunha, P A Fernandes, A Hultqvist, M Edoff, J Leitão, R C Vilão, and P M P Salomé. Advanced Characterization of the effect of front passivation on Cu(In ,Ga)Se2, poster for E-MRS Spring Meeting, 2019.

[CFH+18] J. M.V. Cunha, P. A. Fernandes, A. Hultqvist, J. P. Teixeira, S. Bose, B. Vermang, S. Garud, D. Buldu, J. Gaspar, M. Edoff, J. P. Leitao, and P. M.P. Salome. Insulator Materials for Interface Passivation of Cu(In,Ga)Se2 Thin Films. *IEEE Journal of Photovoltaics*, 8(5):1313–1319, 2018.

[CLB+12] Miguel A. Contreras, Lorelle M. Mansfield, Brian Egaas, Jian Li, Manuel Romero, Rommel Noufi, Eveline Rudiger-Voigt, and Wolfgang Mannstadt. Wide bandgap Cu(In,Ga)Se2 solar cells with

improved energy conversion efficiency. *Progress in Photovoltaics*, 20(7):843–850, 2012.

[Cox09] S F J Cox. Muonium as a model for interstitial hydrogen in the semiconducting and semimetallic elements. *Reports on Progress in Physics*, 72(11):130, 2009.

[Eck91] Wolfgang Eckstein. *Computer Simulation of Ion-Solid Interactions*, volume 10. Springer, 1991.

[EM03] Joel Pantoja Enríquez and Xavier Mathew. Influence of the thickness on structural, optical and electrical properties of chemical bath deposited CdS thin films. *Solar Energy Materials and Solar Cells*, 76(3):313–322, 2003.

[GAD+03] J M Gil, H V Alberto, J Piroto Duarte, N Ayres De Campos, R C Vilão, A Weidinger, M V Yakushev, and S F J Cox. Muon diffusion and trapping in chalcopyrite semiconductors. *Physica B*, 326(1-4):181–184, 2003.

[GAV+99] J M Gil, H V Alberto, R C Vilão, J Piroto Duarte, P J Mendes, L P Ferreira, and N Ayres De Campos. Novel Muonium State in CdS. *Physical Review Letters*, 83(25):5294–5297, 1999.

[GAV+00] J. M. Gil, H. V. Alberto, R. C. Vilão, J. Piroto Duarte, P. J. Mendes, N. Ayres De Campos, A. Weidinger, Ch Niedermayer, M. V. Yakushev, R. D. Pilkington, R. D. Tomlinson, and S. F.J. Cox. High-temperature trapping of muons in CuInSe2 and CuInS2. *Physica B: Condensed Matter*, 289-290:567–569, 2000.

[GLB+19] J. Gaspar, J.P. Leitão, S. Bose, M. Edoff, J.P. Teixeira, J. Borme, W.C. Chen, P.M.P. Salomé, P.A. Fernandes, J.M.V. Cunha, and N.S. Nilsson. A morphological and electronic study of ultrathin rear passivated Cu(In,Ga)Se2 solar cells. *Thin Solid Films*, 671(February):77–84, 2019.

[Gru10] Marius Grundmann. *The Physics of Semiconductors*. Springer, second edition, 2010.

[Gue18] Bernardes Guerreiro. *Beryllium oxide for semiconductor technology*. Master's thesis, Universidade de Coimbra, 2018. https://estudogeral.sib.uc.pt/handle/10316/86129.

[Gug16] Zurab Guguchia. Muon Spin Rotation (uSR) technique and its applications in magnetism and superconductivity. Technical report, Paul Scherrer Institut, 2016. https://www.tsu.ge/data/file_db/faculty_zust_sabunebismetk/Guguchia-Georgia-2016v4.pdf.

[GVPA01] J. M. Gil, R. C. Vilão, J. Piroto Duarte, and N. Ayres de Campos. Shallow donor muonium states in II-VI semiconductor compounds. *Physical Review B*, 64(7):1–8, 2001.

[Hut09] Mark Hutchins. Solar Frontier hits new CIS cell efficiency record, (accessed on 2019-06-09). https://www.pv-magazine.com/2019/01/21/solar-frontier-hits-new-cis-cell-efficiency-record/?utm{_}source=dlvr.it{\&}utm{_}medium=linkedincompanies.

[IEA19] IEA. Snapshot 2019 of Gloval Photovoltaic Market. Technical report, IEA International Energy Agency, 2019. http://www.iea-pvps.org/fileadmin/dam/public/report/statistics/IEA-PVPS_T1_35_Snapshot2019-Report.pdf.

[ISE19] Fraunhofer ISE. Photovoltaics Report. Technical Report March, Fraunhofer ISE, 2019. https://www.ise.fraunhofer.de/content/dam/ise/de/documents/publications/studies/Photovoltaics-Report.pdf.

[LBD+99] W. Liu, M. G. Boshier, S. Dhawan, O. Van Dyck, P. Egan, X. Fei, M. Grosse Perdekamp, V. W. Hughes, M. Janousch, K. Jungmann, D. Kawall, F. G. Mariam, C. Pillai, R. Prigl, G. Zu Putlitz, I. Reinhard, W. Schwarz, P. A. Thompson, and K. A. Woodle. High Preci-

sion Measurements of the Ground State Hyperfine Structure Interval of Muonium and of the Muon Magnetic Moment. *Physical Review Letters*, 82(4):711–714, 1999.

[LES05] O. Lundberg, M. Edoff, and L. Stolt. The effect of Ga-grading in CIGS thin film solar cells. *Thin Solid Films*, 480-481(June):520–525, 2005.

[LWH+13] J. Lindahl, J. T. Wätjen, A. Hultqvist, T. Ericson, M. Edoff, and T. Törndahl. The effect of Zn1-xSnxOy buffer layer thickness in 18.0% efficient Cd-free Cu(In,Ga)Se2 solar cells. *Progress in Photovoltaics: Research and Applications*, 21(8):1588–1597, 2013.

[MGMAGC12] M. A. Muñoz-García, O. Marin, M. C. Alonso-García, and F. Chenlo. Characterization of thin film PV modules under standard test conditions: Results of indoor and outdoor measurements and the effects of sunlight exposure. *Solar Energy*, 86(10):3049–3056, 2012.

[MGP+02] E Morenzoni, H Gluckler, T Prokscha, R Khasanov, H Luetkens, M Birke, E M Forgan, Ch Niedermayer, and M Pleines. Implantation studies of keV positive muons in thin metallic layers. *Nuclear Instruments and Methods in Physics Research Section B: Beam Interactions with Materials and Atoms*, 192(3):254–266, 2002.

[Mol16] Fabien Mollica. *Optimization of ultra-thin Cu(In,Ga)Se2 based solar cells with alternative back-contacts*. PhD thesis, Université Pierre et Marie Curie, 2016. `https://tel.archives-ouvertes.fr/tel-01545671/file/2016PA066556.pdf`.

[Mor09] Elvezio Morenzoni. A (closer) look below surfaces and at heterostructures with polarized muons. *Physica B: Condensed Matter*, 404(5-7):577–580, 2009.

[Mor12] Elvezio Morenzoni. Introduction to µSR: Muon Spin Rotation/Relaxation - Lecture notes, 2012. `https://www.psi.`

ch/sites/default/files/import/lmu/EducationLecturesEN/MuonSpinRotation-An-Introduction-print-em-2012.pdf.

[Mor14] E Morenzoni. Muon science with continuous beams at PSI - Course notes, 2014. https://www.isis.stfc.ac.uk/Pages/2014-morenzoni-psi.pdf.

[MVV+17] A. G. Marinopoulos, R. C. Vilão, R. B.L. Vieira, H. V. Alberto, J. M. Gil, M. V. Yakushev, R. Scheuermann, and T. Goko. Defect levels and hyperfine constants of hydrogen in beryllium oxide from hybrid-functional calculations and muonium spectroscopy. *Philosophical Magazine*, 97(24):2108–2128, 2017.

[Nag03] Kanetada Nagamine. *Introductory Muon Science*. Cambridge University Press, 2003.

[NARA+10] N. Naghavi, D. Abou-Ras, N. Allsop, N. Barreau, S. Bücheler, A. Ennaoui, C. H. Fischer, C. Guillen, D. Hariskos, J. Herrero, R. Klenk, K. Kushiya, D. Lincot, R. Menner, T. Nakada, C. Platzer-Björkman, S. Spiering, A. N. Tiwari, and T. Törndahl. Buffer layers and transparent conducting oxides for chalcopyrite Cu(In,Ga)(S,Se)2 based thin film photovoltaics: Present status and current developments. *Progress in Photovoltaics: Research and Applications*, 18(6):411–433, 2010.

[NRE14] NREL - National Renewable Energy Laboratory. Best Research-Cell Efficiency Chart, (accessed on 2019-06-14). https://www.nrel.gov/pv/cell-efficiency.html.

[NSD14] L. Nuccio, L. Schulz, and A. J. Drew. Muon spin spectroscopy: Magnetism, soft matter and the bridge between the two. *Journal of Physics D: Applied Physics*, 47(47):35, 2014.

[OKA+16] Olindo Isabella, Klaus Jäger, Arno Smets, René van Swaaij, and Miro Zeman. *Solar Energy: The Physics and Engineering of Photovoltaic Conversion, Technologies and Systems*. UIT Cambridge Ltd., 2016.

[ORN+02] Kay Orgassa, Uwe Rau, Quang Nguyen, Hans Werner Schock, and Jürgen H. Werner. Role of the CdS buffer layer as an active optical element in Cu(In, Ga)Se2 thin-film solar cells. *Progress in Photovoltaics*, 10(7):457–463, 2002.

[OSW03] K. Orgassa, H. W. Schock, and J. H. Werner. Alternative back contact materials for thin film Cu(In,Ga)Se2 solar cells. *Thin Solid Films*, 431-432(May):387–391, 2003.

[Pie04] S.M. Pietruszko. Photovoltaics in the World. *Opto-Electronics Review*, 12(1):7–12, 2004.

[PKG+16] Albert Polman, Mark Knight, Erik C. Garnett, Bruno Ehrler, and Wim C. Sinke. Photovoltaic materials: Present efficiencies and future challenges. *Science*, 352(6283), 2016.

[PMD+05] T. Prokscha, E. Morenzoni, K. Deiters, F. Foroughi, D. George, R. Kobler, and V. Vrankovic. A new high-intensity, low-momentum muon beam for the generation of low-energy muons at PSI. *Hyperfine Interactions*, 159(1-4):385–388, 2005.

[PME+07] T. Prokscha, E. Morenzoni, D. G. Eshchenko, N. Garifianov, H. Glückler, R. Khasanov, H. Luetkens, and A. Suter. Formation of hydrogen impurity states in silicon and insulators at low implantation energies. *Physical Review Letters*, 98(22):1–4, 2007.

[Pra00] F L Pratt. WIMDA : a muon data analysis program for the Windows PC. *Physica B: Condensed Matter*, 289-290(August):710–714, 2000.

[PSI31a] PSI. Low Energy Muons: Overview of the Experimental Setup, (accessed on 2019-05-31). `https://www.psi.ch/en/low-energy-muons/experimental-setup`.

[PSI31b] PSI. Low Energy Muons: the Moderator, (accessed on 2019-05-31). `https://www.psi.ch/en/low-energy-muons/moderator`.

[PSI26] PSI. Low-Energy Muon Facility (LEM), (accessed on 2019-06-26). https://www.psi.ch/en/smus/lem.

[PZ03] Clas Persson and Alex Zunger. Anomalous Grain Boundary Physics in Polycrystalline CuInSe2 : The Existence of a Hole Barrier. *Physical Review Letters*, 91(26):266401–1 –266401–4, 2003.

[REN18] REN21. Renewables 2018 Global StatusReport. Technical report, Renewable Energy Policy Network for the 21st Century, 2018. www.ren21.net.

[RS17] Jeyakumar Ramanujam and Udai P. Singh. Copper indium gallium selenide based solar cells - A review. *Energy and Environmental Science*, 10(6):1306–1319, 2017.

[Sal11] Pedro Salomé. *Chalcogenide Thin Films for Solar Cells: Growth and Properties*. PhD thesis, Universidade de Aveiro, 2011. http://hdl.handle.net/10773/3498.

[SFL+14] Pedro M.P. Salomé, Paulo A. Fernandes, Joaquim P. Leitão, Marta G. Sousa, Jennifer P. Teixeira, and António F. Da Cunha. Secondary crystalline phases identification in Cu2ZnSnSe4 thin films: Contributions from Raman scattering and photoluminescence. *Journal of Materials Science*, 49(21):7425–7436, 2014.

[SS11] Roland Scheer and Hans-Werner Schock. *Chalcogenide Photovoltaics*. Wiley-VCH, 2011.

[Ulf09] Ulf Malm and Marika Edoff. Simulating Material Inhomogeneities and Defects in CIGS Thin-film Solar Cells. *Progress in Photovoltaics*, 17(5):306–314, 2009.

[VAG+03] R. C. Vilão, H. V. Alberto, J. M. Gil, J. P. Piroto Duarte, N. Ayres de Campos, A. Weidinger, and M. V. Yakushev. Hydrogen states in CuInSe2 - A μSR study. *Physica B: Condensed Matter*, 340-342:965–968, 2003.

[VAGW19] R C Vilão, H V Alberto, J M Gil, and A Weidinger. Thermal spike in muon implantation. *Physical Review B*, 9(19):1–7, 2019.

[Vil07] R. C. Vilão. *Isolated hydrogen in II – VI zinc – chalcogenide widegap semiconductors modelled by the muon analogue*. PhD thesis, Universidade de Coimbra, 2007. `https://estudogeral.sib.uc.pt/handle/10316/2537`.

[Vil19] R. C. Vilão. Semicondutores e Nanoestruturas - Course notes - Universidade de Coimbra, 2019.

[VVA+17] R. C. Vilão, R. B.L. Vieira, H. V. Alberto, J. M. Gil, and A. Weidinger. Role of the transition state in muon implantation. *Physical Review B*, 96(19):1–7, 2017.

[VVA+18] R. C. Vilão, R. B.L. Vieira, H. V. Alberto, J. M. Gil, A. Weidinger, R. L. Lichti, P. W. Mengyan, B. B. Baker, and J. S. Lord. Barrier model in muon implantation and application to Lu2O3. *Physical Review B*, 98(11):1–9, 2018.

[WGWC07] Stuart R. Wenham, Martin A. Green, Muriel E. Watt, and Richard Corkish. *Applied photovoltaics*. Earthscan, 2nd edition, 2007.

[WKNN01] T Wada, N Kohara, S Nishiwaki, and T Negami. Characterization of the Cu(In,Ga)Se2/Mo interface in CIGS solar cells. *Thin Solid Films*, 387(1-2):118–122, 2001.

[WNA11] WNA. Comparison of Lifecycle Greenhouse Gas Emissions of Various Electricity Generation Sources. Technical report, World Nuclear Assiciation, 2011. `https://www.world-nuclear.org/uploadedFiles/org/WNA/Publications/Working_Group_Reports/comparison_of_lifecycle.pdf`.

Appendix A

Instruction manual

DREAM - Depth REsolved Analysis for Muons, version 1.0, 2019

Description

A MATLAB fitting routine which utilizes the MINUIT [1] minimization engine from CERN has been been developed. It uses the muon stopping probability per unit length in the sample for various implantation energies, simulated with the Monte Carlo code TRIM.SP [2], and the experimental values obtained with the μSR, to fit the experimental data using fit results and depth values as free parameters [3]. The MINUIT engine is used in MATLAB thanks to the Fminuit program developed by Giuseppe Allodi [4], which is an optimization and chi-square fitting program for MATLAB, Octave and Scilab, based on the MINUIT minimization engine. The routine follows the method presented in the accompanying paper [5].

Setting-up

Before running this code it is necessary to first obtain the distribution of particles in a given material, or combination of materials, for a number of implantations energies, using the TRIM.SP code.

The current code is divided in two parts.

First, it loads directly the output files from TRIM.SP, converting them in MATLAB workspace variables, and calculates the muon stopping probability per unit length.

Then, given a set of experimental points, it fits the experimental data to the model presented in [5], based on a set of initial guesses and limited boundaries for the free parameters. While running the code, a set of commands are available in order to allow the user to choose the fitting model. The fitting routine works on the assumption that the implantation energy values, and depth values, are always equally spaced.

Instructions:

- **0.** Do the TRIM.SP simulations for the interface under study (implantation energy typically varies between 1 keV and 28 keV).

- **1.** Place the files obtained from TRIM.SP in the folder TRIM.SP (only the .rge files are strictly needed);

- **2.** Open the folder 'Methods' and open the file calcStopProb.m in order to calculate the muon stopping probability per unit length. Follow the instructions in the routine.

- **3.** A new MATLAB routine must be opened, depending on the number of steps and/or smoothing you want to use to fit the experimental data. To choose the desired option and routine, open the respective subfolder within the folder 'Methods'. The current options are:

  - 2_Steps

  - 3_Steps

  - 4_Steps

  - 5_Steps

  - Smooth_1 – Uses 2 steps with a smooth curve between them;

  - Smooth_2 – Uses 3 steps, with a smooth curve between the second and third steps;

a) Open 'muonFit_...' and 'fitFunction', and follow the instructions presented in the 'muonFit_...'.

- If you are happy with the results, don't forget to store the fitting results. They will be overwritten in a new fit or erased after closing MATLAB.

Code acknowledgments:

1 Minuit routines from CERN: https://root.cern.ch/download/minuit.pdf

2 Wolfgang Eckstein. Computer Simulation of Ion-Solid Interactions, volume 10. Springer, 1991.

3 The Simpson's Rule function present in this code is written by Damien Garcia and taken from the MATLAB File Exchange: https://www.mathworks.com/matlabcentral/fileexchange/25754-simpson-s-rule-for-numerical-integration

4 - Fminuit is an optimization and chi-square fitting program for Matlab, Octave and Scilab, based on the MINUIT minimization engine, developed by Giuseppe Allodi: http://www.fis.unipr.it/ giuseppe.allodi/Fminuit/Fminuit_intro.html

5 " Muon implantation experiments in films : obtaining depth-resolved information", A.F.A. Simões et al, to be submitted (2019).